Physics of Fluids ARTICLE pubs.aip.org/aip/pof

Characterization of nonequilibrium shock interaction in CO_2-N_2 flows over double-wedges with respect to Mach number and geometry

Cite as: Phys. Fluids **35**, 066120 (2023); doi: 10.1063/5.0148436
Submitted: 1 March 2023 · Accepted: 18 May 2023 ·
Published Online: 12 June 2023

C. Garbacz, F. Morgado,[a] and M. Fossati

AFFILIATIONS

Aerospace Centre, Department of Mechanical and Aerospace Engineering, University of Strathclyde, 75 Montrose Street, Glasgow G1 1XJ, United Kingdom

Note: This paper is part of the special topic, Shock Waves.
[a]**Author to whom correspondence should be addressed:** ana.gomes@strath.ac.uk

ABSTRACT

The characterization of the shock interaction mechanism originating from the high-Mach nonequilibrium flow over double-wedge geometries is key to the design of hypersonic vehicles. The impact of changes in the freestream Mach number and double-wedge geometry on the patterns of shock interaction is investigated by means of numerical simulation in the case of CO_2-N_2 flows. The extended laminar Navier–Stokes equations with a two-temperature model to account for translational-to-vibrational internal energy transfer are considered the physical model of this type of flow. Simulations show that reducing the freestream Mach number leads to an increase in the separation region, both in the compression corner and in the locations of shock impingement. The impact of the size of the separation region on the patterns of interaction is such that it causes variations in the type of shock interaction. From the point of view of the flow physics near the wedges, decreasing the freestream Mach number has an equivalent effect to increasing the angle of the second wedge and an opposite effect to increasing the freestream temperature on the pattern of interaction. Results show that decreasing the freestream Mach number leads to an overall reduction in pressure and heating loads along the surface of the wedges and smaller regions of thermal equilibrium behind the bow shock.

I. INTRODUCTION

Shock interaction is a fundamental mechanism of compressible fluid mechanics characterizing many supersonic and hypersonic flows. When such an interaction takes place in the proximity of a wall, shock boundary layer interaction, and consequent flow separation, recirculation and reattachment generate a complex pattern of mechanical and heating loads with high and localized peaks of pressure and heat fluxes. A highly cost-effective and accessible approach to characterizing the interaction mechanisms and predicting the flow physics is computational fluid dynamics, equipped with advanced physical and numerical models to account for the nonequilibrium physical processes taking place in such high-Mach high-enthalpy flows. When a high-enthalpy flow is rapidly decelerated through a shock wave, vibrational and electronic modes of molecules are excited and chemical reactions take place. At high freestream velocities, the relaxation times of these finite-rate processes are comparable to the fluid residence time and a thermochemical nonequilibrium state is established. The nonequilibrium state, also referred to as high-temperature effects, influences the structure of the shock wave system, their interaction, and, in turn, the surface thermo-mechanical loads.[1–3]

The study of the shock interaction mechanism occurring in the proximity of relevant simplified geometries such as double-wedges has been proven instrumental in discovering new physics and better understanding the role of nonequilibrium processes in determining the type of interaction.[4] Additionally, it represents conceptually the deflection of control surfaces or two-dimensional hypersonic intakes. The interaction between a shock formed by the fuselage and the shock generated at the wing of a vehicle can also be modeled as a double-wedge. The type of interaction that occurs depends on specific non-dimensional parameters, which for inviscid flow and calorically perfect gas are the freestream Mach number M, the ratio of specific heats γ, the ratio of the first wedge face length to the second wedge face length L_2/L_1, and the two wedge angles θ_1 and θ_2.[4] In the case of viscous flow, the Reynolds number Re will also influence the pattern of

interaction. When high-temperature effects, such as finite-rate chemistry and thermal nonequilibrium, are present, the freestream temperature is an additional critical parameter, since it has a significant impact on nonequilibrium processes.

Numerous studies on the influence of the geometry on shock interactions have been conducted.[4–8] It has been found that the area of separation created by the compression corner increases and the separation point moves toward the front edge with a larger aft angle.[8] A bigger aft angle led to a greater standoff distance for the bow shock, a greater chance of shock impingement on the wall, and an overall more complicated mechanism of interaction, possibly including instabilities in the shear layers or other unsteady dynamics.[5,8]

Research has been carried out to understand the effect of the gas composition and/or specific heat ratio on the physics of shock interactions.[5,8] Tumuklu *et al.* conducted a comparison of the flow over a 30°–55° double-wedge with three different gas mixtures: air, nitrogen, and argon.[9] It was discovered that the size of the separated region, the upstream movement of the triple-point, and the time to reach a steady state were much smaller for air than for nitrogen. Argon had the quickest movement of the triple-point compared to the other two mixtures. In Ref. 10, it was concluded that the relative magnitude of the specific heat ratio has a significant impact on the SWBLI (Shock Wave/Boundary Layer Interaction). Specifically, the flow of argon resulted in a separation bubble with 1.8 times the size of the one for nitrogen and, due to the endothermic effects of finite-rate chemistry, the size of this region was 1.5 times smaller for air than for nitrogen.

In hypersonic nonequilibrium shock interactions, the freestream temperature has been shown to have a significant impact on the flow patterns.[6,11] Results of previous numerical studies simulating the flow over a double-wedge, for different gas mixtures and freestream temperatures, $T_\infty = 300$ and $T_\infty = 1000$ K, show changes in the shock wave pattern for the case of an air mixture.[11] For the CO_2–N_2 case, weaker shocks leading to a flow pattern that is more attached to the wall were obtained for the larger freestream temperature. However, the change in interaction pattern did not occur. The smaller impact of the freestream temperature on the CO_2-dominated flow was attributed to the much faster vibrational relaxation of CO_2 molecules, as the flows with a CO_2–N_2 mixture revealed overall much smaller discrepancies between translational and vibrational temperature. Similar conclusions concerning the flow of air were drawn in Ref. 6.

The influence of the freestream Mach number has been assessed in Refs. 6 and 12. A computational analysis of an air flow over a double-wedge, with $M_\infty = 7.14$ and $M_\infty = 7.3$, revealed that increasing the freestream Mach number results in later flow separation and larger values of the heat flux peaks at reattachment and impinging shock regions, despite presenting the same qualitative distribution of the surface quantities.[12] In Ref. 6, the freestream Mach number was increased from 2.8 to 9. The resulting flow field was significantly affected, with the larger value of Mach number leading to reduced shock angles, increased real gas effects that further contribute to smaller bow shock standoff distances and a significant rise in pressure.

Continued research effort on achieving better insight into shock interference focuses mostly on flows of air or nitrogen.[1,3–5,7,13–15] This work draws specific attention to CO_2-dominated mixtures, which have become relevant in the aerospace scientific community due to recent Mars exploration programs. The internal structure of the CO_2 three-atomic molecule influences the process of energy redistribution among the different internal modes and, in turn, the macroscopic properties of the flow. Previous work[16] compared inviscid flow over a double-wedge geometry for mixtures of air and CO_2, using the two-temperature model by Park.[17] Results have confirmed that different molecular structures and behavior of nonequilibrium finite-rate processes have a significant impact on the obtained shock interaction patterns and associated surface loads. To better understand nonequilibrium shock interaction physics in CO_2-dominated flows, the authors recently investigated the impact of increasing the aft wedge angle as well as the impact of using different thermo-physical models for the mixture, comparing the flow patterns obtained with Park's two-temperature model to those obtained with thermally perfect and perfect ideal gas models. Increasing the aft angle significantly enlarged the separated region in the compression corner, which lead to the generation of a larger number of shock waves and shear layers. Except for the case of the maximum angle, where the strongest peaks were owing to shock impingement, heat flux, and pressure peaks with increasing intensity occurred along the surface due to boundary layer reattachment downstream of the compression corner. The size of the recirculation bubble at the compression corner, the shock interaction mechanism, and the surface loads were all shown to be heavily influenced by the different assumptions on vibrational mode excitation. When the model assumed a larger portion of the internal energy being absorbed by the vibrational mode (the respective order being perfect ideal gas → two-temperature gas → thermally perfect gas), lower post-shock temperatures were obtained, which increased post-shock density, resulting in weaker shock interactions characterized by delayed onsets of separation, reduced separation regions, and smaller bow shock standoff distance.

After investigating the effect of freestream temperature, geometry, and physical modeling on the nonequilibrium CO_2 flow over the double-wedge,[11] this work aims to investigate the response of the hypersonic shock wave system to changes in the values of Mach number in the freestream flow. Numerical simulations are performed for a viscous flow over four different double-wedge geometries (15°–40°, 15°–45°, 15°–50°, and 15°–55°) and three different values of the freestream Mach number (7, 9, and 11). This article is organized as follows: Sec. II introduces the flow physics of hypersonic flow over double-wedges and Sec. III presents the governing equations and physical and numerical models adopted in this work. Section IV presents the double-wedge geometry together with the computational domain and boundary conditions. Section V presents the parametric study of the nonequilibrium shock interaction mechanisms with respect to the freestream Mach number over four different geometries, and Sec. VI elaborates on the role of nonequilibrium in defining the shock interaction mechanism. In Sec. VII, the main conclusions are summarized.

II. SHOCK INTERACTION PATTERNS OVER DOUBLE-WEDGES

The flow over a double-wedge geometry is mostly dictated by the presence of two compression corners. When the supersonic freestream encounters the first wedge's leading edge, an oblique shock forms, deflecting the streamlines according to the wedge's angle. Another oblique shock is generated at the second compression corner. Depending on the freestream flow conditions, the lengths and angles of the two wedges, and the characteristics of the gas, the flow patterns

arising from the interference of these two oblique shocks will result in different shock interaction mechanisms.

Figure 1 shows the schematic of two different inviscid shock interactions: type VI and type V.[13] In the type VI interaction, the flow is purely supersonic and the oblique shock waves originating at the two corners, the leading shock (LS) and the corner shock (CS), directly intersect at point P. As a result, a contact discontinuity (CD) occurs, which distinguishes the flow that has traveled through both shocks, LS and CS, from the flow that has only passed through the bow shock (BS). An expansion wave (EW) is emitted from the oblique shock intersection and reflected on the surface of the second wedge. The type V interaction is characterized by one triple point P, where shock LS, shock BS, and transmitted shock (TS) intersect. The latter shock interacts with the oblique shock CS generated by the corner between the two wedges, in a shock reflection structure:[19] the TS reflects as shock RS1 and shock CS reflects as shock RS2, which in turn reflects on the surface of the second wedge. The reflection of the two shocks from opposite families, CS and TS, is one of the key features in the type V interaction. Furthermore, a CD is generated at the triple point P and, as a consequence of the reflection of shock RS1 in the contact discontinuity, an EW forms and reflects on the surface of the second wedge.

When viscous effects are present, shock waves and contact discontinuities are no longer discontinuities but take the form of high-gradient regions, which may have a substantial impact on how the flow develops. The presence of a nonequilibrium thermal boundary layer generates a gradient of temperature near the wall, resulting in surface aerodynamic heating. The inclusion of viscous effects in the simulation of this type of flow generates additional flow features such as boundary layers, recirculation zones, and vortices. The interaction between different shock waves and the flow features arising from viscous effects leads to increasingly complex flow physics that may result in localized severe peaks of pressure and heat flux along the surface. As the boundary layer develops along the surface of the fore wedge, the adverse pressure gradient resulting from the presence of the second wedge interacts with the boundary layer, potentially causing flow separation ahead of the corner (schematic at the top of Fig. 2). The flow then reattaches at a certain location on the aft wedge surface and a recirculation bubble is formed below the slip line. This bubble acts as a new wedge, since the supersonic flow over the slip line is forced to adopt the new velocity direction. Figure 2 (top) shows a conceptual sketch of the key features expected in the proximity of the corner. In addition to the presence of a separation/detachment shock wave, reattachment of the boundary layer leads to a series of compression waves that may coalesce and form another shock. At the reattachment point, the boundary layer becomes very thin and the pressure is high, resulting in a region of very high aerodynamic heating.[20] Additionally, the shock wave interaction over the double-wedge may result in shock impingement on the surface, as illustrated at the bottom of Fig. 2. Given the presence of viscous effects, the impinging shock interacts with the boundary layer (SBLI), introducing an adverse gradient of pressure. If this interaction is strong enough, it may cause the boundary layer to separate in the vicinity of the impingement point, generating additional separation and reattachment shocks.

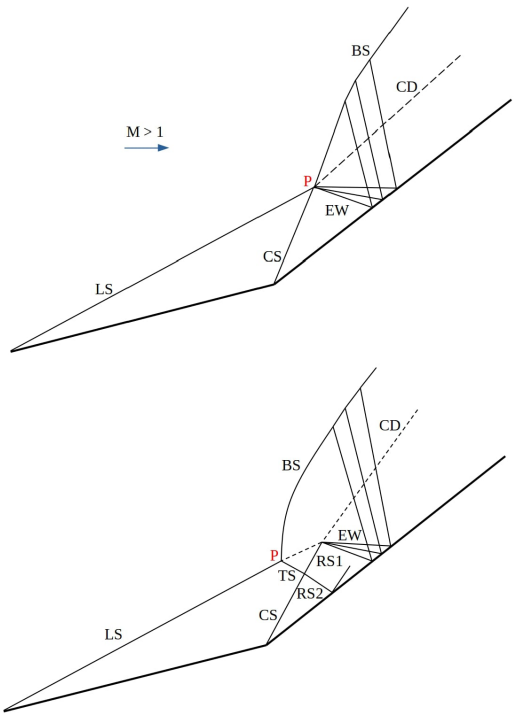

FIG. 1. Examples of shock interaction patterns. Type VI (top), type V (bottom). Reproduced with permission from Garbacz *et al.*, AIAA Paper No. 2022-3277 (2022). Copyright 2022 by the American Institute of Aeronautics and Astronautics.[18]

III. PHYSICAL AND NUMERICAL MODELING

A. Governing equations

The system of equations considered for the present work is the classical extension of the Navier–Stokes equations for a viscous

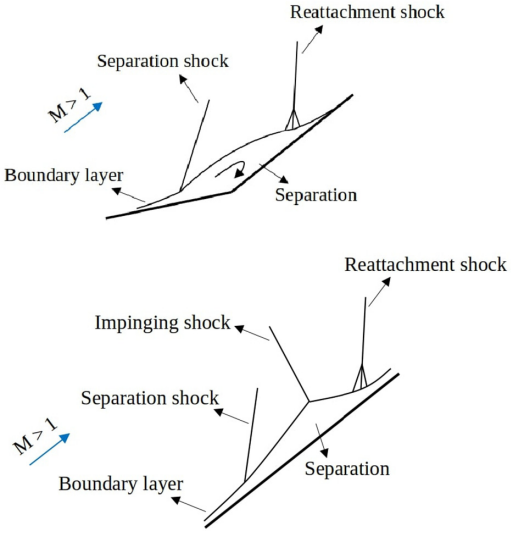

FIG. 2. Shock-boundary layer interaction patterns. Compression corner recirculation bubble and shock wave system (top), shock wave system in the case of boundary layer separation due to shock impingement on the surface (bottom). Reproduced with permission from Garbacz *et al.*, AIAA Paper No. 2022-3277 (2022). Copyright 2022 by the American Institute of Aeronautics and Astronautics.[18]

chemically reacting flow in thermal nonequilibrium adopting one conservation equation per each one of the species in the mixture and a macroscopic multi-temperature approach to account for thermal nonequilibrium.[21] The two-temperature model by Park is used to model the finite-rate internal energy exchange. It was initially developed for air[17] but later modified for CO_2 flows[22] and validated in more recent works against experimental data and the more detailed state-to-state approach.[23,24] The model assumes that rotational relaxation is very fast relative to the rate of fluid motion and therefore considers that the translational and rotational modes of the gas are in equilibrium with each other at the translational-rotational temperature T_{tr}. The CO_2 molecule has three vibrational modes, one of which is double degenerate. Camac[25] showed that all three modes relax at the same time, but considerably slower than the rate of fluid motion, leading to a single separate temperature to describe this process. Electronic modes are assumed to be at equilibrium with vibration; therefore, it is considered that these two modes relax at the vibrational-electronic temperature T_{ve}. In a compact form, the system of equations can be described as

$$\frac{\mathrm{d}\mathbf{U}}{\mathrm{d}t} + \nabla \cdot \vec{\mathbf{F}}^{\mathrm{c}}(\mathbf{U}) = \nabla \cdot \vec{\mathbf{F}}^{\mathrm{v}}(\mathbf{U}) + \mathbf{Q}(\mathbf{U}), \tag{1}$$

where the conservative variables, convective fluxes, viscous fluxes, and source terms are given by

$$\mathbf{U} = \begin{Bmatrix} \rho_1 \\ \vdots \\ \rho_{n_s} \\ \rho\vec{u} \\ \rho e \\ \rho e^{\mathrm{ve}} \end{Bmatrix}, \quad \vec{\mathbf{F}}^{\mathrm{c}} = \begin{Bmatrix} \rho_1\vec{u} \\ \vdots \\ \rho_{n_s}\vec{u} \\ \rho\vec{u}\otimes\vec{u} + p\bar{I} \\ \rho h\vec{u} \\ \rho e^{\mathrm{ve}}\vec{u} \end{Bmatrix},$$

$$\vec{\mathbf{F}}^{\mathrm{v}} = \begin{Bmatrix} \vec{J}_1 \\ \vdots \\ \vec{J}_{n_s} \\ \bar{\tau} \\ \bar{\tau}\cdot\vec{u} + \sum_s \vec{J}_s h_s + \vec{q}^{\mathrm{ve}} + \vec{q}^{\mathrm{tr}} \\ \sum_s \vec{J}_s h_s^{\mathrm{ve}} + \vec{q}^{\mathrm{ve}} \end{Bmatrix}, \quad \mathbf{Q} = \begin{Bmatrix} \dot{\omega}_1 \\ \vdots \\ \dot{\omega}_{n_s} \\ 0 \\ 0 \\ \dot{\Omega} \end{Bmatrix} \tag{2}$$

and ρ is the density of the mixture, ρ_s is the partial density of species s, $\vec{u}$ is the flow velocity vector, $\dot{\omega}_s$ is the chemical source of species s, $\dot{\Omega}$ is the vibrational energy source term, p is the static pressure, e and e^{ve} are, respectively, the total energy per unit mass and the vibrational energy per unit mass for the mixture, h is the total enthalpy per unit mass, $\vec{J}_s$ is the species mass diffusion flux, $\bar{\tau}$ is the viscous stress tensor, $\vec{q}$ is the conduction heat flux, index s denotes the sth chemical species and n_s is the total number of species. A mixture of 10 species is considered: $CO_2/N_2/C/N/O/C_2/O_2/CN/CO/NO$ with the reaction mechanism taken from Park *et al.*[22]

Calculating the nonequilibrium thermodynamic state and source terms is necessary to close the system of governing equations that describes hypersonic flows. This is achieved by means of coupling with appropriate multi-temperature thermochemistry models. The equations presented below describe the implementation of the two-temperature model for a mixture composed of neutral species, provided by the Mutation++ library.[26] Each individual species s is assumed to behave as an ideal gas. Hence, the total pressure of the mixture p is defined by Dalton's law as the summation of the partial pressures associated with each species p_s, determined by the ideal gas law,

$$p = \sum_{s=1}^{n_s} p_s = \sum_{s=1}^{n_s} \rho_s \frac{R_{\mathrm{u}}}{M_s} T_{\mathrm{tr}}, \tag{3}$$

where R_{u} is the universal gas constant, M_s is the molar mass of species s, and T_{tr} is the translational-rotational temperature. The total specific energy of the flow e is given as the sum of the internal and kinetic energies,

$$e = \sum_{s=1}^{n_s} c_s e_s + \frac{1}{2}\vec{u}\cdot\vec{u}, \tag{4}$$

where c_s is the mass fraction of species s and e_s is the specific internal energy of the species, given by the sum of the energy of formation e_s^0 and the contribution of each internal mode (t-translational, r-rotational, v-vibrational, e-electronic),

$$e_s = e_s^{\mathrm{t}}(T_{\mathrm{tr}}) + e_s^{\mathrm{r}}(T_{\mathrm{tr}}) + e_s^{\mathrm{v}}(T_{\mathrm{ve}}) + e_s^{\mathrm{e}}(T_{\mathrm{ve}}) + e_s^0. \tag{5}$$

In the two-temperature model, the energy transfer mechanisms that determine the change in vibrational energy of the mixture, are accounted for in the source term vector. The source term $\dot{\Omega}$ is defined as the sum of the translational-to-vibrational energy transfer and energy exchanges due to chemical activity,

$$\dot{\Omega} = \sum_{s=1}^{n_s} \dot{\Omega}_s^{\mathrm{tr:ve}} + \dot{\Omega}_s^{\mathrm{c:v}} + \dot{\Omega}_s^{\mathrm{c:e}}. \tag{6}$$

The term $\dot{\Omega}^{\mathrm{tr:ve}}$ concerns the rate of energy exchange between the translational and vibrational energy modes, following the Landau–Teller model:[27]

$$\dot{\Omega}_s^{\mathrm{tr:ve}} = \rho_s \frac{e_s^{\mathrm{v}}(T) - e_s^{\mathrm{v}}(T_{\mathrm{v}})}{\tau_s^{\mathrm{V-T}}}. \tag{7}$$

The vibrational relaxation time of each species, $\tau_s^{\mathrm{V-T}}$, is given by the Millikan and White empirical formula[28] and the Park correction.[29]

The change in vibrational-electronic energy of the mixture due to the production/destruction of species is accounted for in the terms $\dot{\Omega}_s^{\mathrm{c:v}}$ and $\dot{\Omega}_s^{\mathrm{c:e}}$, given by Scoggins,[30]

$$\dot{\Omega}_s^{\mathrm{c:v}} = c_1 \dot{\omega}_s e_s^{\mathrm{v}}, \quad \dot{\Omega}_s^{\mathrm{c:e}} = \dot{\omega}_s e_s^{\mathrm{e}}. \tag{8}$$

A non-preferential dissociation model is considered to account for the coupling between vibrational energy modes and finite-rate chemistry. The model assumes that molecules are destroyed or created at the average vibrational energy of the cell, $c_1 = 1$.

Finite-rate chemistry is accounted for by considering a mass conservation equation for each species in the gas, incorporating a production/destruction term that results from chemical activity. The chemical source term $\dot{\omega}_s$ is given by

$$\dot{\omega}_s = M_s \sum_{r=1}^{n_r} (\nu''_{s,r} - \nu'_{s,r}) \left[k_{\mathrm{f},r} \prod_{j=1}^{n_s} \hat{\rho}_j^{\nu'_{j,r}} - k_{\mathrm{b},r} \prod_{j=1}^{n_s} \hat{\rho}_j^{\nu''_{j,r}} \right], \tag{9}$$

where n_r and n_s are, respectively, the number of reactions and the number of species, ν'_s is the forward reaction stoichiometry coefficient, ν''_s is the backward reaction stoichiometry coefficient, $\hat{\rho}_j$ is the molar density, $k_{f,r}$ is the forward reaction rate, and $k_{b,r}$ is the backward reaction rate. The forward reaction rate for each reaction r is defined according to the modified Arrhenius equation.[31]

With regard to dissipative fluxes, the mass diffusion flux of each species $\vec{J}_s$ is described by Fick's Law of diffusion,

$$\vec{J}_s = \rho_s \vec{V}_s, \tag{10}$$

where $\vec{V}_s$ is the element diffusion velocity, obtained by solving the Stefan–Maxwell equations under the Ramshaw approximation. The viscous stress tensor is written in vector notation as

$$\bar{\tau} = \mu\left(\nabla\vec{u} + \nabla\vec{u}^{\mathsf{T}} - \frac{2}{3}\bar{I}(\nabla\cdot\vec{u})\right), \tag{11}$$

where μ is the mixture viscosity coefficient. The conduction heat flux for each thermal energy mode $\vec{q_k}$ is assumed to be given by Fourier's Law of heat conduction,

$$\vec{q_k} = \lambda_k \vec{\nabla}(T_k), \tag{12}$$

where T_k is the temperature and λ_k is the thermal conductivity coefficient of the kth energy mode. Viscosity μ and mode thermal conductivity λ_k are computed using Wilke's mixing rule.[32] The species thermal conductivity is calculated using Eucken's formula[33] that takes into account both translational and vibrational temperatures.

B. Numerical framework

The multi-species and multi-temperature Navier–Stokes equations are solved numerically with the open-source CFD code SU2-NEMO[34] (NonEquilibrium MOdels). SU2-NEMO has been developed for the purpose of simulating chemically reactive and nonequilibrium flows and has been extensively validated.[35] The external library Mutation++ (Refs. 26 and 36) (Multicomponent And Thermodynamic Transport properties for IONized gases in C++) provides efficient algorithms for the computation of thermodynamic, transport (viscosity, thermal conductivity, and diffusion) and chemical kinetic gas properties for a given state of the mixture. The library has been designed for robustness over a wide range of temperatures and is accurate in dealing with multi-temperature models. SU2-NEMO implements a finite-volume edge-based formulation and for this work, the AUSM scheme[37] (Advection Upstream Splitting Method) together with MUSCL (Monotonic Upstream-centered Scheme for Conservation Laws) and the Venkatakrishnan-Wang limiter have been used to achieve a second order in space discretization of the convective fluxes, while the diffusive fluxes are discretized by means of a standard second-order accurate central scheme. The CFL number was tailored to each test-case to allow for solution convergence, varying in a range 0.1–0.75. A dual time-stepping approach with a second-order backward-difference discretization is used for unsteady flows.

C. Code validation

Despite the large number of experimental studies carried out to validate the numerical modeling of hypersonic flows with mixtures of air and nitrogen, little work has focused on the specific mixture of CO_2 studied in this work. To the best of the authors' knowledge, there are no experiments at all on carbon-dioxide shock interactions. In this section, three cases are presented as means to validate the framework introduced in Secs. III A and III B. The first case aims at validating the capability of the employed models to reproduce the physics of shock interactions, and a mixture of air is considered. The simulation of a viscous hypersonic flow over a proximal-sphere configuration is considered.[38] The shock interaction originates from the impingement of the bow shock generated by the leading sphere on the bow shock in front of the secondary sphere. The freestream flow conditions, wall temperature, and species mass fractions for the simulation are written in Table I.

TABLE I. Freestream and wall values for the two-sphere case.

T_∞ (K)	55.56
T_w (K)	293.15
P_∞ (Pa)	125.61
V_∞ (m/s)	1048
$Y\,[\mathrm{N}]_\infty$	0
$Y[\mathrm{O}]_\infty$	0
$Y[\mathrm{NO}]_\infty$	0
$Y[\mathrm{N_2}]_\infty$	0.77
$Y[\mathrm{O_2}]_\infty$	0.23

A comparison between the numerical Schlieren and experimental Schlieren obtained from experiments is shown in Fig. 3. By overlaying the Schlieren images at the region of the shock-shock interaction, it can be visualized the clear superposition of the experimental and numerical shock waves, supporting the validity of SU2-NEMO to perform shock interaction simulations.

The following validation case refers to the two-dimensional wedge placed symmetrically in a uniform hypersonic flow of reacting carbon dioxide. The hypersonic flow over this simple geometry leads to the appearance of a shock wave that is detached for large enough half-wedge angles. The validation case is taken from the work of

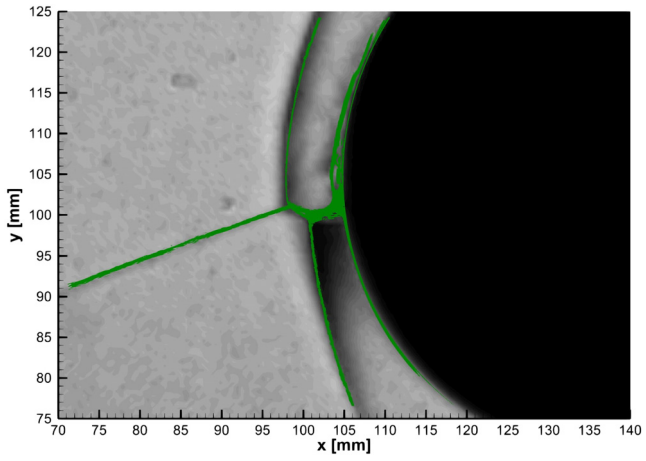

FIG. 3. Experimental and numerical Schlieren in green at the shock–shock interaction region.[39]

TABLE II. Freestream conditions for the wedge simulation.

M_∞	6
P_∞ (Pa)	2441.5
T_∞ (K)	1960
$Y[C]_\infty$	0
$Y[N]_\infty$	0
$Y[O]_\infty$	0.07
$Y[C_2]_\infty$	0.0
$Y[N_2]_\infty$	0.0
$Y[O_2]_\infty$	0.176
$Y[CN]_\infty$	0
$Y[CO]_\infty$	0.428
$Y[NO]_\infty$	0.0
$Y[CO_2]_\infty$	0.326

Hornung and Smith,[40] who have performed experiments using a symmetric finite-length wedge model of varying half-angle. Numerical reference data are also available from two-dimensional simulations performed by Candler.[41] The freestream conditions used in the study are shown in Table II.

Figure 4 shows a comparison of bow shock standoff distance data for different half-wedge angles. Numerical results obtained with SU2-NEMO are validated against experimental data[40] and verified against simulations performed by Candler.[41] The shock standoff distance is measured in the stagnation line, where nonequilibrium effects are expected to be more pronounced. Results obtained with SU2-NEMO are found to be in satisfactory agreement with the other two sets of data, with the case of the stronger bow shock (for a half-wedge angle of 65°) showing the largest discrepancy against both numerical and experimental reference values. The differences seen between experimental and SU2-NEMO data can be explained in part due to the effect of the finite transverse length of the 3D model used in the experiments. The mechanism of reaction used in SU2-NEMO, as seen in Table II, allows for reactions involving nitrogen, which could lead to production of chemical species that are not found in the experiment. The discrepancies between data obtained with SU2-NEMO and numerical data provided by Candler[41] can also be attributed to the different mechanism of reaction considered, as well as other code-to-code differences in terms of physical and numerical modeling.

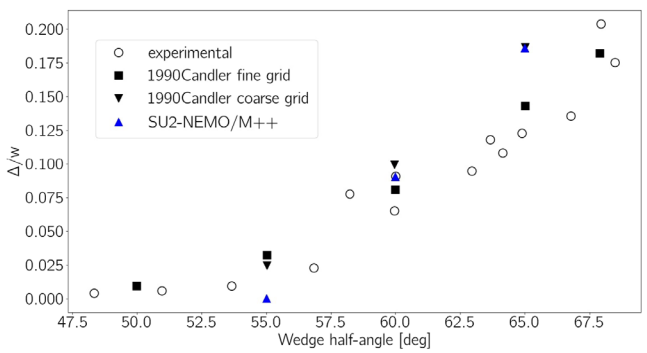

FIG. 4. Comparison of normalized shock standoff distance between numerical and experimental data.

TABLE III. Double-cone freestream conditions.

M_∞	4.41
P_∞ (Pa)	12 300
T_∞ (K)	1530
$Y[O_2]_\infty$	0.1152
$Y[O]_\infty$	0.0038
$Y[CO_2]_\infty$	0.6726
$Y[CO]_\infty$	0.2084
$Y[C]_\infty$	0.0
$Y[C_2]_\infty$	0.0

The last validation case investigates the carbon-dioxide high-speed flow over the 25°–55° double-cone, taken from Ref. 42. The flow over a double-cone configuration typically results in a complex shock-shock and shock-boundary-layer interaction which is known to be sensitive to thermal and chemical nonequilibrium. The freestream conditions are indicated in Table III. Numerical results obtained with SU2-NEMO for an axisymmetric simulation are compared with available data for surface heat flux measurements of the laminar boundary layer and with numerical predictions obtained with the DPLR code.[43]

Contours of Mach number obtained with SU2-NEMO are shown in Fig. 5. In agreement with the experimental results of Knisely, the CO_2 flow over the double-cone results in a type V shock interaction pattern. The surface heat flux profile characterizing this type of interaction can be broken down into four general sections: the laminar boundary layer, separated flow region, reattachment-impingement region, and post-reattachment region. Given the transitional nature of the flow reported in the experimental investigation, for the purpose of this verification/validation exercise, the comparison of surface heat flux profiles is performed for the laminar portion of the boundary layer. In Fig. 6, data obtained with SU2-NEMO are compared against experimental measurements and numerical results obtained with the DPLR code. For the latter, the axisymmetric simulation was performed for a single cone geometry (equivalent to simulating the laminar flow region in the double-cone case). Very good agreement is found

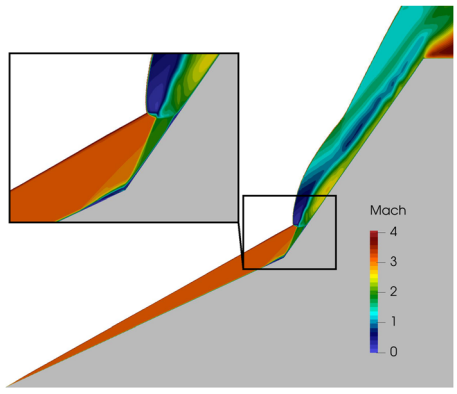

FIG. 5. Contours of Mach number for the CO_2 flow over the double-cone.

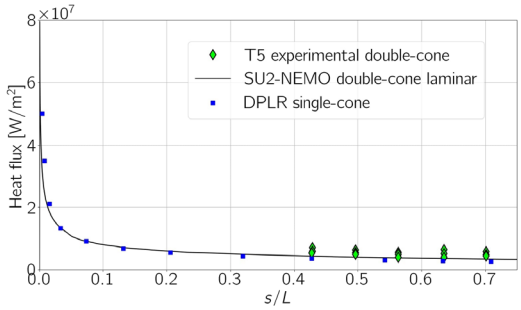

FIG. 6. Comparison of surface laminar heat flux predictions with experimental data.

between all three sets of data, demonstrating the accuracy of SU2-NEMO and its coupling with the Mutation++ library in predicting hypersonic flow physics using CO_2-based mixtures.

D. Grid independence

The supersonic flow over a double-wedges generates a complex environment that includes shock waves, boundary and shear layers, etc. These features are very localized, highly directional and characterized by sharp gradients. Anisotropic mesh adaptation is considered to ensure the flow physics revealed by the study is not affected by poor choices of grid resolution. This type of grid adaptation is carried out via node clustering and element edge alignment with flow features rather than by simply adding more nodes. For the structured near-wall region, adaptation is done by means of tangential and normal clustering/increasing of nodes. The Mach number is chosen as the flow variable driving the adaptation process. Grid convergence is assessed qualitatively, on the basis of the observation of well-defined types of shock interaction following the classification paradigm originally introduced by Edney.[13] A quantitative assessment performed by comparing the temperature profile normal to the wall in the main region of shock interaction (this location is indicated in Fig. 7 with a red line), normalized wall surface pressure and wall surface heat flux. A grid convergence study was performed for all test-cases, but only the case of the flow over a 15°–55° double-wedge with $M_\infty = 11$ is reported here to illustrate the approach adopted. The original isotropic hybrid mesh and the final adapted anisotropic hybrid mesh are shown in Fig. 7. Quantitative comparisons for the different iterations of adaptation are shown in Fig. 8. Results obtained for meshes 2 and 3 are

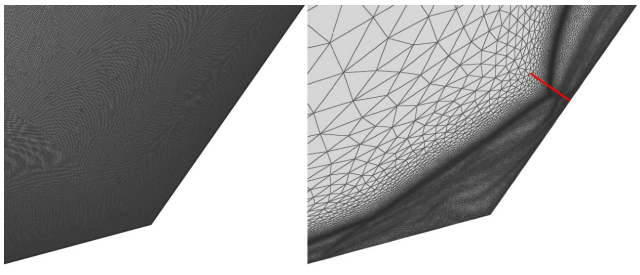

FIG. 7. Original and final adapted meshes for the case of the 15°–55° double-wedge with $M_\infty = 11$.

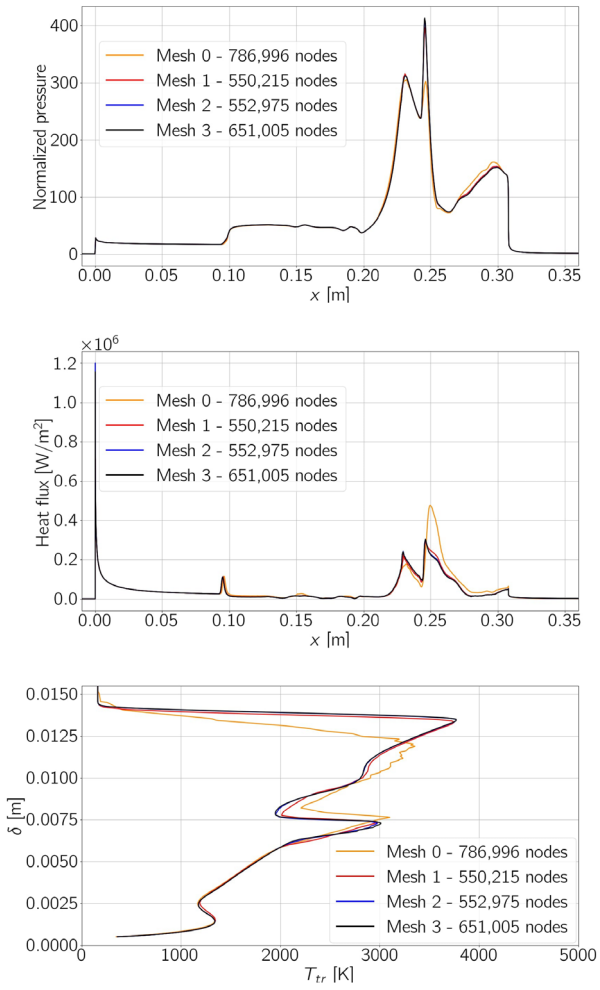

FIG. 8. Grid convergence study for the case of the 15°–55° double-wedge with $M_\infty = 11$. Normalized surface pressure (top), heat flux (middle), and temperature normal to the wall (bottom). Reproduced with permission from Garbacz *et al.*, AIAA Paper No. 2022-3277 (2022). Copyright 2022 by the American Institute of Aeronautics and Astronautics.[18]

essentially superimposed for all quantities. Table IV provides the number of nodes of the final grids used for each test-case.

IV. PROBLEM SETUP AND TEST MATRIX

The double-wedge geometry considered in this study is illustrated in Fig. 9. Four different configurations are considered with a fixed fore angle of $\theta_1 = 15°$ and aft angles θ_2 of 40°, 45°, 50°, and 55°. Previous work[18] published by the authors of this paper refers to the cases 45° and 55° and serves as the basis for the current parametric study. For all cases, $L_1 = L_2 = 0.2$ m. The two wedge surfaces and the expansion surface downstream of the expansion corner are assumed to be isothermal walls. For the leftmost horizontal segment, a symmetry boundary condition is applied. An outlet boundary condition is chosen for the exit, and farfield is considered for the remaining boundaries. Numerical simulations are performed for a flow of CO_2:97%, N_2:3% referring to the atmosphere of Mars. Simulation parameters,

TABLE IV. Number of grid nodes of used in the final mesh of each test-case.

	$M_\infty = 11$	$M_\infty = 9$	$M_\infty = 7$
15°–40°	526 679	475 209	378 256
15°–45°	374 324	530 124	478 233
15°–50°	498 411	422 547	489 396
15°–55°	651 005	458 391	1 090 778

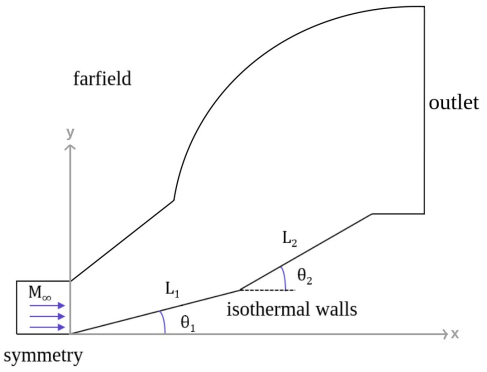

FIG. 9. Double-wedge geometry, computational domain, and boundary conditions. Reproduced with permission from Garbacz *et al.*, AIAA Paper No. 2022-3277 (2022). Copyright 2022 by the American Institute of Aeronautics and Astronautics.[18]

presented in Table V, are chosen so that the freestream conditions are in the laminar continuum regime and values of pressure and temperature that can be found in the Martian atmosphere. The freestream flow is assumed to be in thermal equilibrium.

TABLE V. Simulation parameters.

M_∞	p_∞ (Pa)	T_∞ (K)	T_{wall} (K)	Mole fractions
7, 9, 11	10	160	300	CO_2: 0.97, N_2: 0.03

V. PATTERN IDENTIFICATION FOR VARYING FREESTREAM MACH

A. 15°–40° double-wedge

Figure 10 shows contours of the Mach number and difference between translational and vibrational temperatures (which measures thermal nonequilibrium) for the flow over the 15°–40° double-wedge for decreasing freestream Mach number: 11, 9, 7. The white line in the top row refers to the sonic line. All three cases display a type VI interaction, characterized by the direct interaction of two oblique shocks that results in a combined shock BS, an EW and a CD or slip layer when viscous effects are present (inviscid schematic provided at the top of Fig. 1).

It is well known from inviscid gas dynamics that, in a flow over a wedge, increasing the freestream Mach number causes the oblique attached shock wave, or the detached bow shock, to move closer to the body. For the case of an attached shock, a shock that is closer to the body is associated with a lower shock angle. In Fig. 11(a) (top), Mach contour lines for the three cases are plotted. It is clearly seen that for shock LS, which occurs only due to the presence of the first wedge, the shock angle continuously increases with decreasing Mach number, following the expected trend. The boundary layer along the surface of the first wedge is increasingly thicker for lower freestream Mach, as a result of the lower post-leading-shock flow velocity in this region.

As the freestream Mach number is decreased from 11 to 7, shock CS has a larger shock angle, which in turn gives rise to a larger pressure gradient interacting with the boundary layer. Looking at Fig. 10,

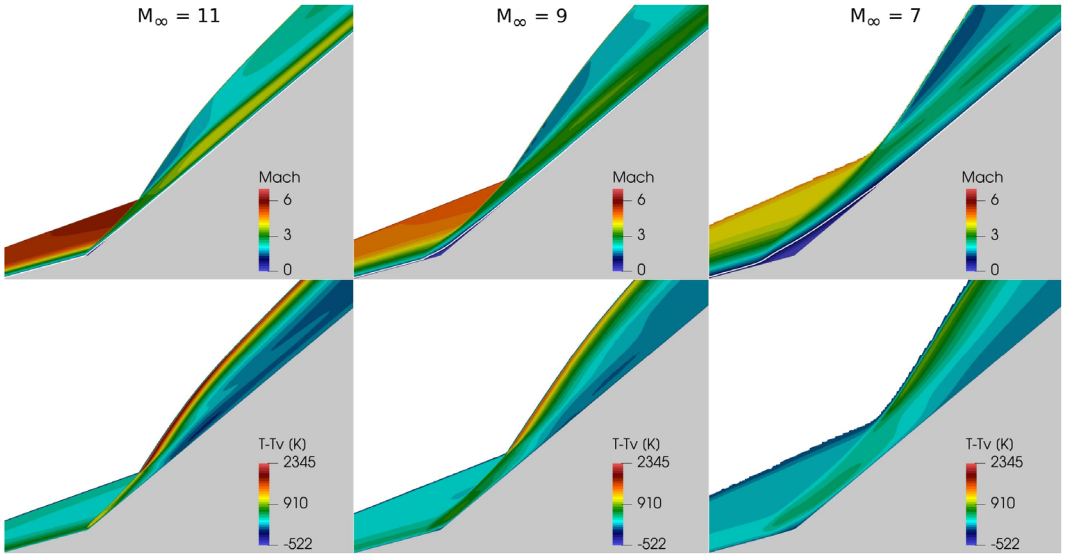

FIG. 10. Contours of Mach number (top) and difference between translational and vibrational temperatures (bottom) for a CO_2–N_2 flow over the 15°–40° double-wedge with $M_\infty = 11$, $M_\infty = 9$, and $M_\infty = 7$.

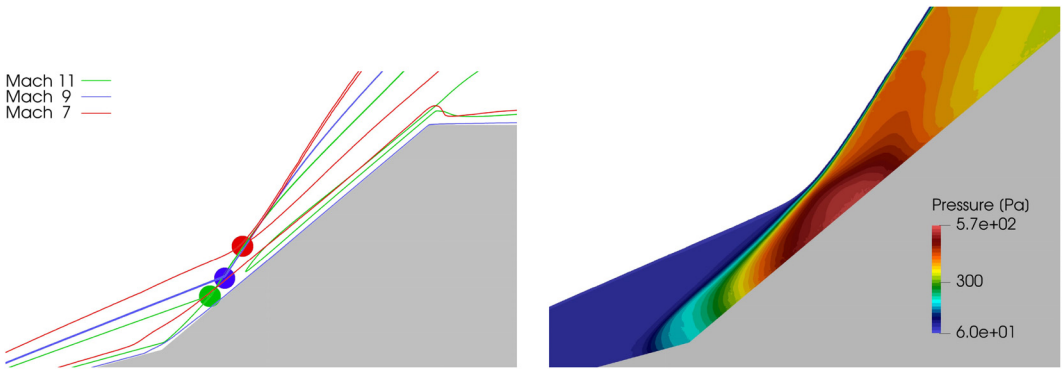

FIG. 11. Comparison of Mach number contour lines for different values of freestream Mach (7, 9, 11) for the 15°–40° geometry (top). Contours of pressure for a CO_2-N_2 flow over the 15°–40° double-wedge with $M_\infty = 7$ (bottom).

the main difference in the flow occurs in the compression corner, in the region of boundary layer detachment. The larger adverse pressure gradient traveling upstream through the thicker boundary layer causes the detachment point to occur further upstream for decreasing values of freestream Mach. Larger separation, as well as subsonic regions (indicated by the white line in the top row of Fig. 10), result from the lower freestream Mach. For all three cases, the size of the separated flow region is small enough that no reattachment shock occurs. Instead, the gradual reattachment of the boundary layer results in a series of compression waves that coalesce into the detachment shock, which can be visualized clearly at the bottom side of Fig. 11(a), showing pressure contours for a zoomed view of the compression corner for the case of $M_\infty = 7$. The detachment shock interacts directly with shock LS at the triple-point P, generating features BS, EW and a viscous slip layer. The contour lines displayed at the left side of Fig. 11(a) for all three cases show that the triple-point P tends to travel downstream and further away from the wall as the Mach number decreases. Following the trend observed for the leading shock, the bow shock standoff distance also increases with lower freestream Mach number.

Figure 12 shows the distribution of surface quantities, normalized pressure, and Stanton number. As expected, lower values of freestream Mach number result in lower distributions of pressure and Stanton number along the whole surface of the geometry. From the surface pressure distribution, the single stage of flow compression at the wall seen for $M_\infty = 9$ and $M_\infty = 11$ is an indication of the coalescence of the boundary layer detachment and reattachment into one single shock. For the case of $M_\infty = 7$, two stages of compression, resulting from detachment and subsequent reattachment of the boundary layer, can been seen. The two stages of gradual compression somewhat merge into each other and still result in a single shock. The increasing size of the separated flow region with decreasing Mach number is shown by two elements for the case of $M_\infty = 7$: (1) the first increase in pressure resulting from flow separation occurs earlier and (2) the maximum value of pressure, corresponding to the point of reattachment, occurs further downstream, compared to the other two cases.

The increasing size of the separated flow region with decreasing Mach number is more evident in the wall Stanton number distribution, shown by the sudden drop of this coefficient after the initial gradual decrease along the surface of the first wedge. For the case of $M_\infty = 11$, the size of the separated region is extremely small and the sudden Stanton number drop is shown by an inverted spike at $x = 0.1932$ m. Whereas the cases for $M_\infty = 9$ and $M_\infty = 7$ exhibit a qualitatively similar distribution that reflects the flow separation in the compression corner followed by gradual flow reattachment and subsequent expansion, the case for $M_\infty = 11$ is slightly more complex. There is a first spike occurring at the point of boundary layer separation. Even though the separated boundary layer is usually associated with decreasing heat flux, by visualizing contours of translational temperature and the sonic line with a close-up near the compression corner, at the left side of Fig. 13, it can be seen that the detachment shock first compresses the flow against the wall just upstream the compression corner at the point of separation, $x = 0.1927$ m—which causes the

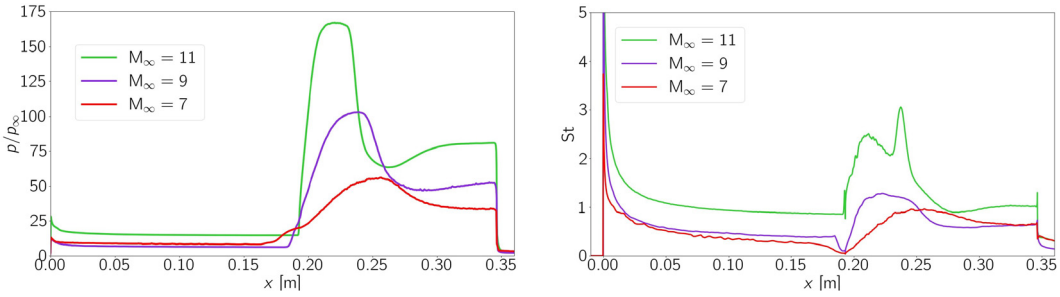

FIG. 12. Comparison of surface quantities distribution for different freestream Mach numbers for the 15°–40° geometry: Normalized pressure (left), Stanton number (right).

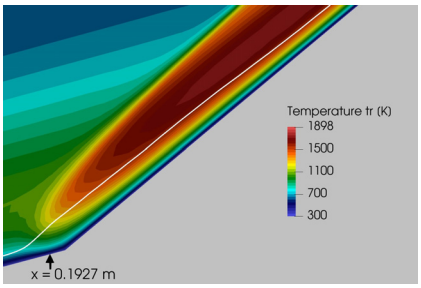

FIG. 13. Compression corner detailed view of the 15°–40° double-wegde with $M_\infty = 11$: translational temperature with sonic line.

wall Stanton number to spike up at this location. Immediately downstream, where the boundary layer is already detached from the wall, the Stanton number decreases suddenly due to presence of the compression corner, leading to the subsequent inverted spike seen at $x = 0.1932$ m. The Stanton number then starts gradually increasing until reaching the wide peak of approximately 2.5 at $x = 0.212$ m, resulting from the gradual reattachment of the boundary layer (indicated by the sonic line that gradually gets closer to the wall, at the left of Fig. 13).

From the contours of Mach number, the Stanton number would be expected to gradually decrease up to the expansion corner, due the expansion wave. However, the maximum peak of Stanton number of around 3 is actually seen for $x = 0.2375$ m. To determine the cause of this maximum value in surface heating, Fig. 14 shows the distribution along the wall of the second wedge of each one of the contributions to the total heat flux, vibrational and translational, at the left. A peak of heat flux is seen for both contributions at $x = 0.2375$ m. To better understand what gives rise to these peaks, profiles of both temperatures have been extracted parallel to the surface of the second wedge, at different normal distances from the wall 0.001, 0.0005, 0.000 25, and 0.0001 m. The temperature profiles are plotted at the right of Fig. 14. For h = 0.001 m, a single peak of translational temperature is seen at $x = 0.2$ m, corresponding to the temperature rise occurring in the reattachment region due to flow compression in the vicinity of the compression corner. After the rise in temperature due to the corner shock, a vibrational-to-translaional energy exchange process initiates and the translational temperature gradually decreases, while the vibrational temperature increases, reaching a peak at $x = 0.234$ m. At this location, the translational temperature starts decreasing more drastically, due to the presence of the expansion wave. As the normal distance to the wall decreases, both temperatures tend to approach 300 K, given the isothermal boundary condition enforcing thermal equilibrium at the wall, with $T_{tr} = T_{ve} = 300$ K. In the direction normal to the surface of the second wedge, toward the wall, for the same x location, internal energy exchange between the translational and vibrational mode occurs to satisfy the condition of thermal equilibrium at the wall. The more detailed analysis leads to the conclusion that the peak of heat flux seen at $x = 0.2375$ m is a combined effect of the expansion wave resulting from the shock interaction and the process of vibrational relaxation.

B. 15°–45° double-wedge

Figure 15 shows contours of Mach number and difference between translational and vibrational temperatures for the flow over the 15°–45° double-wedge for decreasing freestream Mach number: 11, 9, 7. All three cases show the type VI pattern of interaction (top of Fig. 1). Whereas the Mach 11 flow results in the same mechanism of shock interaction as for the case of the 40° aft wedge angle (a single type VI interaction), the Mach 9 and 7 flows exhibit two instances of a type VI interaction. The more complex pattern of interaction for the two latter cases is due to the boundary layer separation occurring further upstream along the surface of the first wedge for lower Mach numbers. As per the discussion for the 15°–40° Case, lower freestream Mach number results in a thicker boundary layer along the surface of the first wedge, which leads to earlier flow separation. The separation bubble is larger and so is the angle of the detachment shock, as well as the distance between the points of flow detachment and reattachment. As the detachment shock interacts with the leading shock, the first type VI pattern of interaction is formed. Further downstream, the combined shock resultant from the latter interaction, in turn, interacts with the shock generated at the flow reattachment point on the surface of the second wedge, leading to another type VI mechanism of interaction.

In Fig. 16, Mach contour lines for the three cases are plotted. Similarly to the 15°–40° geometry, it is seen that, for shock LS, the shock angle continuously increases with decreasing Mach number, following the expected trend. Due to the different patterns of interaction resulting from different values of freestream Mach, for shock BS, this trend is only verified further downstream, where there is less influence of the mechanism of shock interaction. As for the 15°–40° double-wedge, the triple-point P travels downstream and further away from the wall as Mach number decreases. The sonic line in Fig. 15 indicates

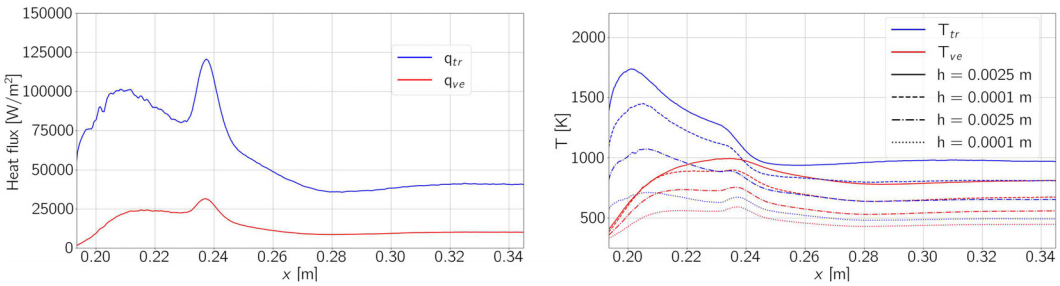

FIG. 14. Detailed analysis of translational and vibrational heat flux contributions (left) and temperatures (right) along the surface of the second wedge, for the 15°–40° double-wedge with $M_\infty = 11$.

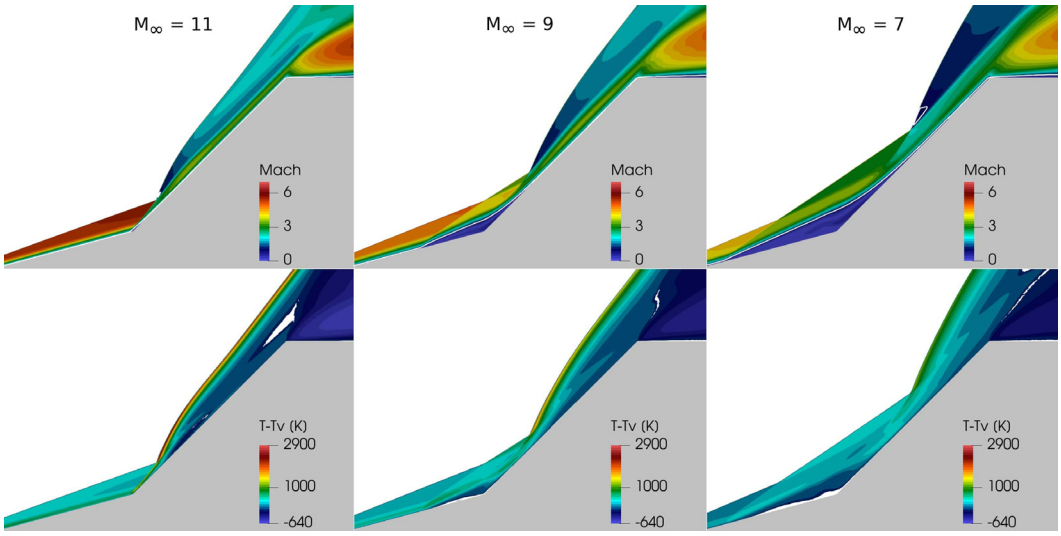

FIG. 15. Contours of Mach number (top) and difference between translational and vibrational temperatures (bottom) for a CO_2-N_2 flow over the 15°–45° double-wedge with $M_\infty = 11$, $M_\infty = 9$, and $M_\infty = 7$. White regions in the bottom row represent thermal equilibrium. Reproduced with permission from Garbacz *et al.*, AIAA Paper No. 2022-3277 (2022). Copyright 2022 by the American Institute of Aeronautics and Astronautics.[18]

that, besides the boundary layer, subsonic flow regions are found behind the bow shock for $M_\infty = 11$ and $M_\infty = 7$. A type VI interaction that results in subsonic pockets behind the bow shock has been named as supercritical type VI by Olejniczak *et al.*[4] A very small subsonic pocket is seen just downstream the triple-point P for $M_\infty = 11$, whereas no subsonic flow exists behind the BS for $M_\infty = 9$. Even though it is expected that a lower freestream Mach number $M_\infty = 9$ would lead to lower post-shock velocities, and eventually a larger subsonic region than for $M_\infty = 11$, this is not the case. As mentioned before, the very small region of flow separation in the case of $M_\infty = 11$ generates one single shock resulting from detachment and subsequent reattachment of the boundary layer. Because these two stages of flow compression are combined into one shock, the associated shock strength and angle are larger than for the detachment shock in the case of $M_\infty = 9$, that is generated only due to boundary layer detachment. As a consequence, there is a larger curvature of BS near the triple-point P for $M_\infty = 11$, leading to the lower and subsonic velocities. From $M_\infty = 9$ to $M_\infty = 7$, which result in the same interaction pattern, the expected trend of lower post-shock velocities obtained for lower freestream Mach number is obtained, with a subsonic pocket being generated for the lower freestream Mach $M_\infty = 7$.

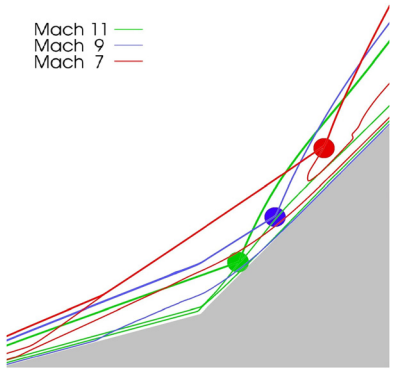

FIG. 16. Comparison of Mach number contour lines for different values of freestream Mach (7, 9, 11) for the 15°–45° geometry. Reproduced with permission from Garbacz *et al.*, AIAA Paper No. 2022-3277 (2022). Copyright 2022 by the American Institute of Aeronautics and Astronautics.[18]

Figure 17 shows the distribution of surface quantities, normalized pressure and Stanton number. For the case of $M_\infty = 11$, both distributions qualitatively follow what was obtained for the 15°–40° geometry and same value of freestream Mach. The cases of $M_\infty = 9$ and $M_\infty = 7$ present a different qualitative distribution from the previous geometry, but identical between each other for the 15°–45° geometry, confirming that both cases result in a type VI interaction. An initial increase/decrease in pressure/Stanton number is seen at approximately $x = 0.09$ and $x = 0.135$ m, for $M_\infty = 9$ and $M_\infty = 7$, respectively, corresponding to the point of boundary layer separation. Further downstream, the peaks of pressure and Stanton number seen at $x = 0.23$ and $x = 0.255$ m, respectively, are associated with the reattachment of the boundary layer. The parametric study shows that, for lower freestream Mach numbers, the larger separated regions reattach more gradually, which is indicated by the significantly wider peaks of pressure and Stanton number.

C. 15°–50° double-wedge

Figure 18 shows contours of Mach number (top row), difference between translational and vibrational temperatures (middle row) and pressure in a zoomed view on the region of interaction (bottom row) for the flow over the 15°–50° double-wedge for decreasing freestream Mach number: 11, 9, and 7. As the aft wedge angle increases from 45° to 50°, for each value of freestream Mach number, the separated flow region in the compression corner continuously thickens, resulting a reattachment shock characterized by a larger shock angle. The bow

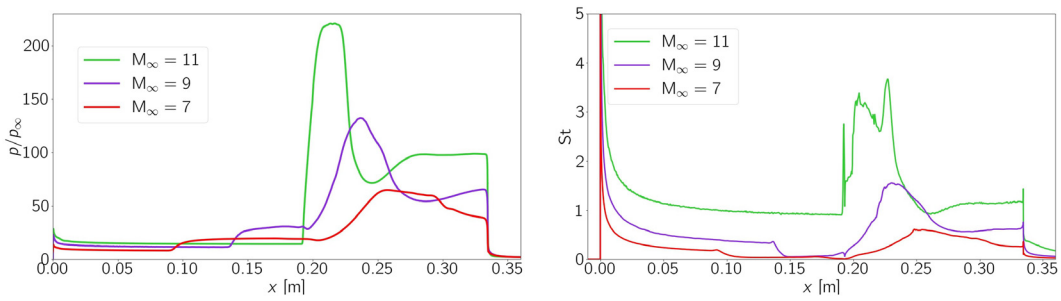

FIG. 17. Comparison of surface quantities distribution for different freestream Mach numbers for the 15°–45° geometry. Normalized pressure (left), Stanton number (right). Reproduced with permission from Garbacz *et al.*, AIAA Paper No. 2022-3277 (2022). Copyright 2022 by the American Institute of Aeronautics and Astronautics.[18]

shock becomes stronger and has a wider standoff distance. From the previous geometry, the way the shock interaction mechanism develops reflects the latter changes, leading to a transition between type VI and type V for the cases of $M_\infty = 11$ and $M_\infty = 9$ and to a fully established type V (bottom of Fig. 1) for $M_\infty = 7$.

Compared to $M_\infty = 9$, the pattern of interaction obtained for $M_\infty = 11$ is closer to the supercritical type VI. Looking at the pressure contours in Fig. 18, the case of $M_\infty = 11$ appears to generate a pattern of interaction corresponding to the system of two shock waves interacting, leading to a combined shock BS, an EW and a slip layer—which would correspond to the type VI interaction. However, the accentuated curvature of the bow shock near the triple-point and the subsonic pocket behind it (white line in the Mach contours) suggests a transition to the type V pattern.[44] For $M_\infty = 9$, the mechanism of interaction displays additional flow features and shocks that are difficult to visualize in the Mach contours but become evident in the zoomed view of the pressure contours. Specifically, the reattachment shock is reflected as shock RS2 (with pressure contours changing from

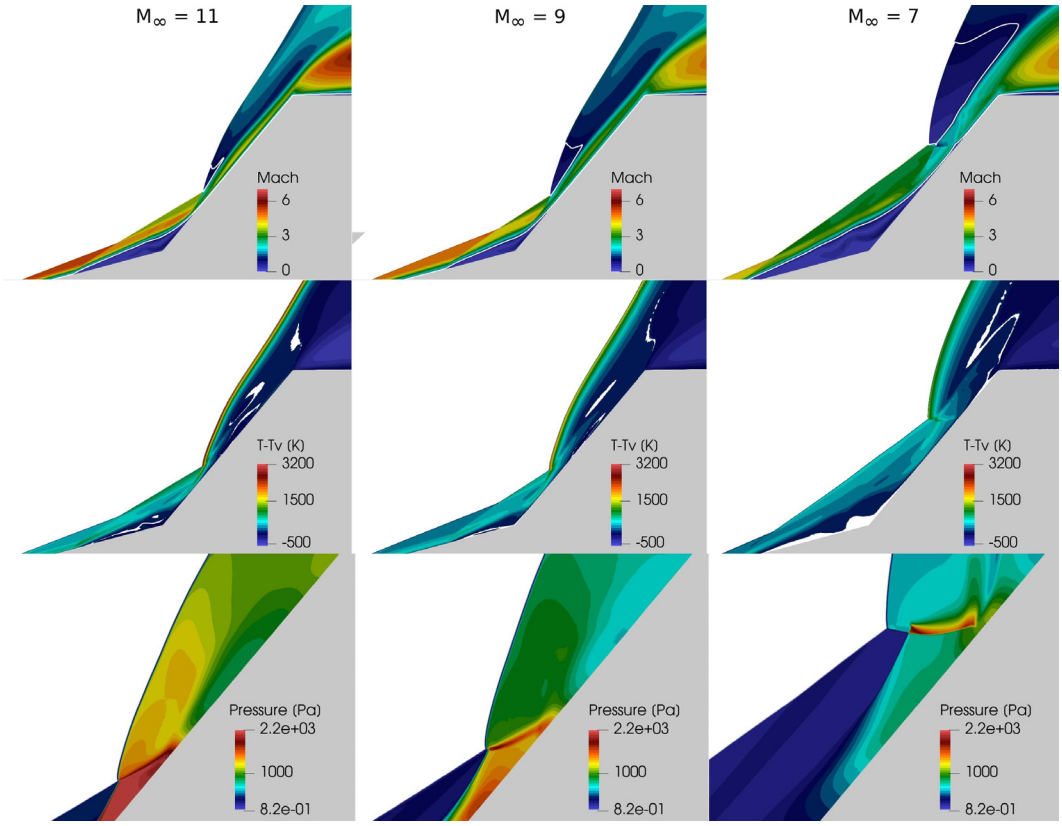

FIG. 18. Contours of Mach number (top), difference between translational and vibrational temperatures (bottom) and pressure (bottom) for a CO_2-N_2 flow over the 15°–50° double-wedge with $M_\infty = 11$, $M_\infty = 9$, and $M_\infty = 7$. White regions in the bottom row represent thermal equilibrium.

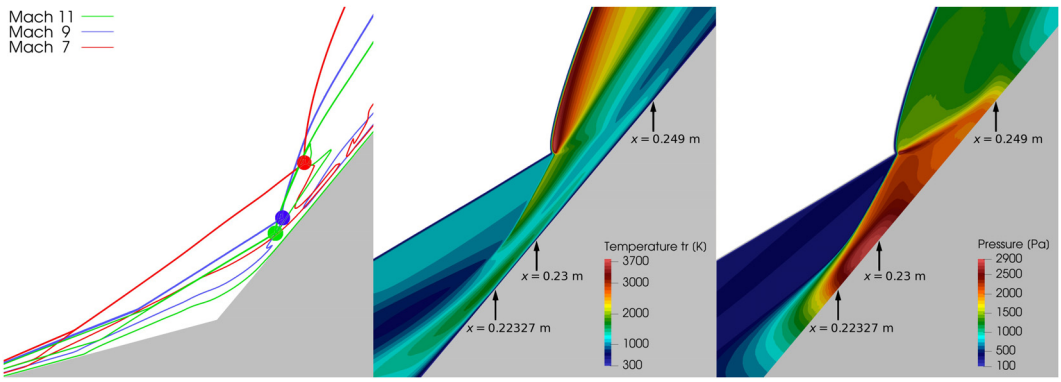

FIG. 19. Comparison of Mach number contour lines for different values of freestream Mach (7, 9, 11) for the 15°–50° geometry (left). Detailed view of the shock interaction region for the 15°–50° double-wegde with $M_\infty = 11$ (middle—translational temperature, right—pressure).

orange to dark red), which, in turn, impinges on the surface of the second wedge.

When the freestream Mach number is further decreased to 7, a more complex interaction system is obtained due to the larger number of shock waves. From Fig. 19 (left), it is seen that the significantly larger separated flow region, as well as significantly larger angle of the detachment shock, cause the triple-point to travel further downstream. The stronger shocks in the main region of interaction, characterized by larger shock angles, push the triple-point further away from the wall. From the triple-point, a transmitted shock is generated and reflected on the reattachment shock, in a regular reflection shock system corresponding to the type V interaction (pressure contours). Another key feature of this pattern of interaction is the impingement of shock RS2 on the surface of the aft wedge (check schematic at the bottom of Fig. 2). This flow feature results in a SWBLI that is strong enough to cause boundary layer separation (indicated by the sonic line in the Mach contours) and, therefore, generate additional separation and detachment shocks. The detachment shock is seen in the pressure contours in the transition from sage green to dark green, and the reattachment shock is indicated by the transition from dark green to lime green—both near the surface of the aft wedge, in the region of shock impingement.

Figure 20 shows a comparison of surface properties for all 15°–50° cases: Mach 11, 9, and 7. For $M_\infty = 11$, up until the pressure peak, the surface pressure distribution follows what is expected from a standard type VI interaction: the first increase in pressure corresponding to the separation of the boundary layer and the peak reflecting the subsequent reattachment. Before the flow fully expands along the surface of the aft wedge, another very small local pressure peak is seen at $x = 0.248$ m. This is an indicator that the flow pattern is not a standard type VI, but instead is transiting to a type V. This small pressure peak is indicative of the flow compression associated with a very weak shock impinging on the surface—weak enough that cannot be visualized in the flow contours, but still affects the surface distributions. When it comes to surface heating, the initial drop of Stanton number at $x = 0.11$ m reflects the point of boundary layer separation. Further downstream, the Stanton number distribution exhibits a few fluctuations, reflecting the recirculating flow inside the separation region. The reattachment of the boundary layer then causes the Stanton number to spike up to approximately 4 at $x = 0.223\,27$ m. At this location, a maximum of translational temperature is also visualized in the contours shown at the middle image of Fig. 19. The contours of pressure shown at the left of the same figure confirm that this the region of compressing flow due to reattachment of the boundary layer. The Stanton number stays approximately constant up to $x = 0.23$ m, and then starts decreasing due flow expansion downstream the point of reattachment (pressure contours from red to orange along the wall). Another spike is seen further downstream at $x = 0.249$ m, this latter spike being due to the weak shock impinging on the surface of the aft wedge. The Stanton number then gradually decreases along the wall up to the expansion corner.

The surface distribution for the case of $M_\infty = 9$ is quite similar to the one for $M_\infty = 11$, confirming that both cases result in a similar

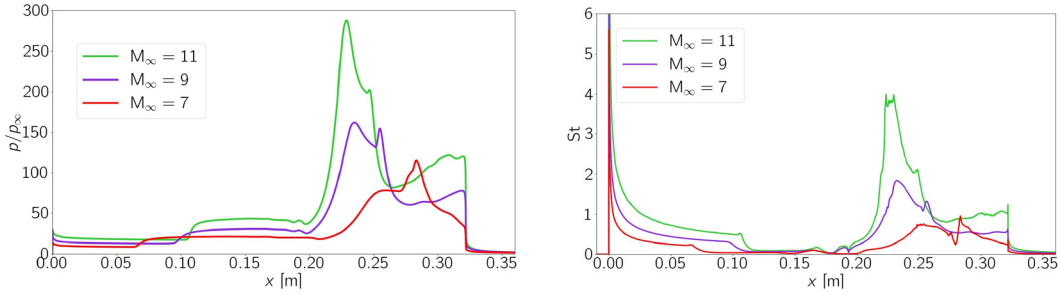

FIG. 20. Comparison of surface quantities distribution for different freestream Mach numbers for the 15°–50° geometry. Normalized pressure (left), Stanton number (right).

mechanism of shock interaction. The fact that $M_\infty = 9$ results in a transition type VI–type V that is closer to the fully established type V interaction is shown by the second spike of pressure. Whereas for $M_\infty = 11$, the weak impinging shock leads to a surface pressure spike that is 0.7 times smaller than reattachment peak, for $M_\infty = 9$, the compression associated with the impinging shock is comparable to the one caused by boundary layer reattachment. The Stanton number distribution for the $M_\infty = 9$ case reflects the aforementioned behavior, where instead this quantity drops in the region of flow separation.

For $M_\infty = 7$, the significantly longer separated flow region and gradual reattachment is evident in both surface pressure and Stanton number distributions. Compared to the two previous cases, $M_\infty = 7$ results in qualitatively different distributions that reflects, instead, the fully established type V interaction pattern. Specifically, after the boundary layer reattachment downstream of the compression corner (that occurs approximately between $x = 0.21$ and $x = 0.26$ m), the surface pressure distributions shows two stages of compression, that would correspond to the detachment and reattachment shocks caused by the SWBLI on the aft wedge's surface (the reattachment shock corresponding to the peak of pressure distribution). The two stages of compression are not easily distinguished in the pressure distribution. However, they become evident in the Stanton number plot, where the separation is shown by the sudden drop at $x = 0.279$ m and the following spike at $x = 0.283$ m reflects flow reattachment downstream of the shock impingement and its interaction with the boundary layer.

D. 15°–55° double-wedge

For the 15°–55° double-wedge, all three values of freestream Mach number result in a type V interaction pattern (bottom of Fig. 1). The $M_\infty = 7$ did not reach a steady state, therefore the solution obtained with the steady state solver was provided as a first guess to resolve the unsteady shock interaction process with time-accurate simulations. Figure 21 shows contours of Mach number and difference between translational and vibrational temperatures for the flow over the 15°–55° double-wedge for freestream Mach numbers 11 and 9. Figure 22 shows the Mach number contours for the $M_\infty = 7$ case. In this figure, contours are shown for four different instants of time, where the first and fourth instant of time depict essentially the same shock interaction pattern, showing that the flow is periodic in time.

The type V interaction pattern is characterized by the reflection of two shocks from opposite families. For the solutions presented in this section, this reflection occurs between the reattachment shock and the transmitted shock generated at the triple-point. This reflection can be a regular reflection RR or a Mach reflection MR, where an additional normal shock connects the points of reflection. For $M_\infty = 11$ and $M_\infty = 9$, a type V interaction with RR reflection is obtained. The pattern of interaction, including the flow features resulting from the presence of viscous effects, is similar. The differences between $M_\infty = 11$ and $M_\infty = 9$ follow the trends observed for the previous geometries. A larger recirculation bubble in the compression corner is obtained for the lower Mach number, which in turn results in a leading shock and detachment shock characterized by larger angles—see Fig. 23. A larger subsonic region is seen behind the bow shock (see Fig. 24), that is also characterized by a larger standoff distance for the lower Mach number. The most significant differences in the mechanism of interaction are in the main region of shock interference, that is zoomed in in Fig. 24. In this region, for both cases there is shock

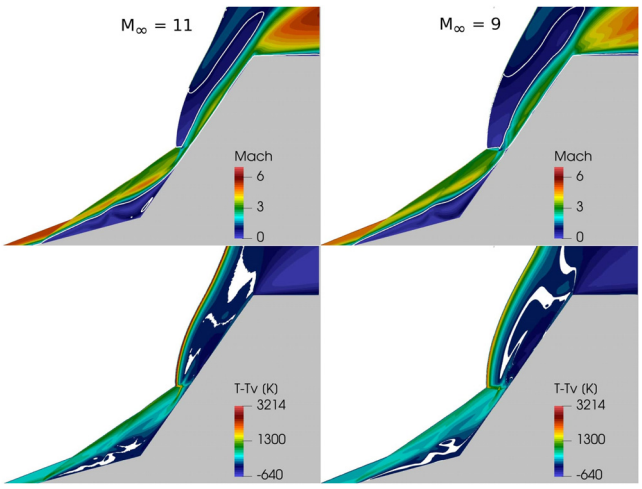

FIG. 21. Contours of Mach number (top) and difference between translational and vibrational temperatures (bottom) for a CO_2-N_2 flow over the 15°–55° double-wedge with $M_\infty = 11$ and $M_\infty = 9$. White regions in the bottom row represent thermal equilibrium. Reproduced with permission from Garbacz *et al.*, AIAA Paper No. 2022-3277 (2022). Copyright 2022 by the American Institute of Aeronautics and Astronautics.[18]

impingement (explained at the bottom of Fig. 2) on the wall of the aft wedge. For the $M_\infty = 9$ case, the impinging shock is stronger and characterized by a larger shock angle, which results in a stronger SBLI. For the $M_\infty = 11$ case, the shock induced boundary layer separation is quite small and does not generate any additional shocks. For $M_\infty = 9$, the separation resulting from shock impingement is larger enough to generate additional detachment and reattachment shocks occurring upstream and downstream of the separation point, respectively. The two shocks can be clearly visualized in the pressure

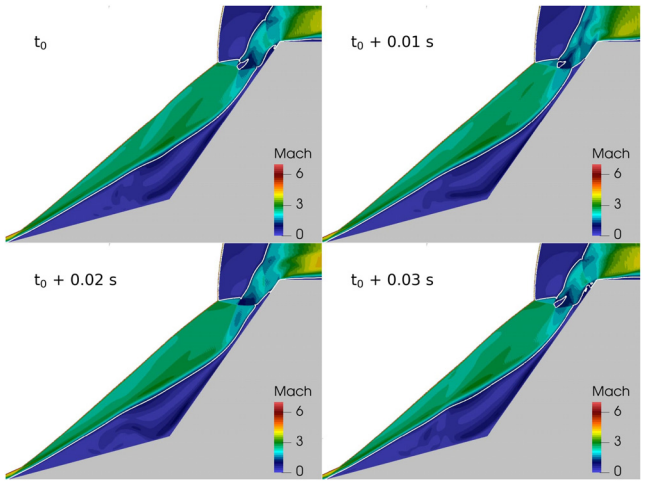

FIG. 22. Contours of Mach number for a CO_2-N_2 with $M_\infty = 7$ flow over the 15°–55° double-wedge. Reproduced with permission from Garbacz *et al.*, AIAA Paper No. 2022-3277 (2022). Copyright 2022 by the American Institute of Aeronautics and Astronautics.[18]

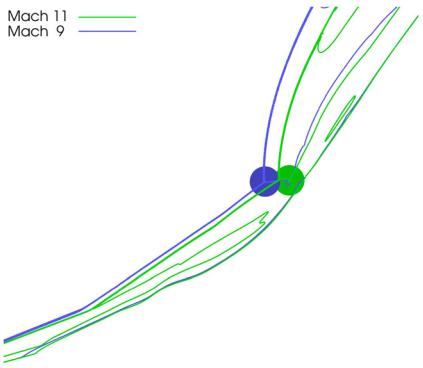

FIG. 23. Comparison of Mach number contour lines for different values of freestream Mach (9, 11) for the 15°–45° geometry. Reproduced with permission from Garbacz *et al.*, AIAA Paper No. 2022-3277 (2022). Copyright 2022 by the American Institute of Aeronautics and Astronautics.[18]

contours of the bottom row in Fig. 24, from the transition of light blue to green contours (detachment shock) and green to yellow contours (reattachment shock). It is concluded that a more complex shock interaction pattern, with a larger number of interacting shock waves, is obtained for the $M_\infty = 9$ case. By looking at Fig. 23, from the locations of both triple-points, it can be extrapolated that when separation from shock impingement occurs, the main region of interaction is pushed upstream. Since a larger separation due to shock impingement is obtained for $M_\infty = 9$, the triple-point is therefore located more upstream than for $M_\infty = 11$. It is relevant to notice that this trend is opposite of what was seen for the previous geometries.

The $M_\infty = 7$ case results in a periodic mechanism of shock interaction. The periodicity of the flow can be seen in the matching patterns of interaction between the first and fourth instant of time in Fig. 22. Comparing to the larger values of freestream Mach number, $M_\infty = 11$ and $M_\infty = 9$, the separation bubble increases significantly. The shock angles are also much larger and the location of the triple-point is substantially further downstream, toward the expansion corner. Instead of the steady type V regular reflection pattern obtained for $M_\infty = 11$ and $M_\infty = 9$, the stronger shocks lead to an oscillating type V pattern that continuously changes between a Mach reflection and a regular reflection of the reattachment and transmitted shocks. It is relevant to notice that, for this case, very large regions of the domain result in subsonic flow. Similarly to the previous cases, subsonic velocities are found in the separated boundary layer, near the compression corner as well as location of shock impingement, and behind the bow shock. For $M_\infty = 7$, an additional subsonic pocket is seen behind the Mach stem, for the first, second and fourth instants of time.

Periodic mechanisms of shock interaction have been analyzed before in various works.[5,7,8,45] Unsteadiness in the viscous type V interaction has been explained by the strong coupling between the recirculation bubble, the impinging shock and the bow shock. As the reflected shock impinges on the surface of the aft wedge and separates the boundary layer, the resulting adverse pressure gradient travels upstream through the subsonic portion of the boundary layer, and feeds the vortex dynamics inside the recirculation bubble. As the main region of interaction travels downstream, the impinging shock becomes weaker, the vortex energy inside the separation bubble decays and the motion of the whole shock system changes direction.

Figure 25 shows the instantaneous distribution of surface quantities for the 15°–55° double-wedge with $M_\infty = 7$ case. The periodicity of the flow pattern is here confirmed by the matching distributions of normalized pressure and Stanton number for the instants of time t_0 and $t_0 + 0.03$ s. In the normalized surface pressure plot, it can be seen that, between t_0 and $t_0 + 0.01$ s, the point of impingement travels downstream and the pressure peak intensity decreases. At $t_0 + 0.02$ s, this effect is further emphasized, and the reattachment shock already travels slightly upstream, which would correspond to the stage of decaying vortex energy (the reattachment shock is indicated by the

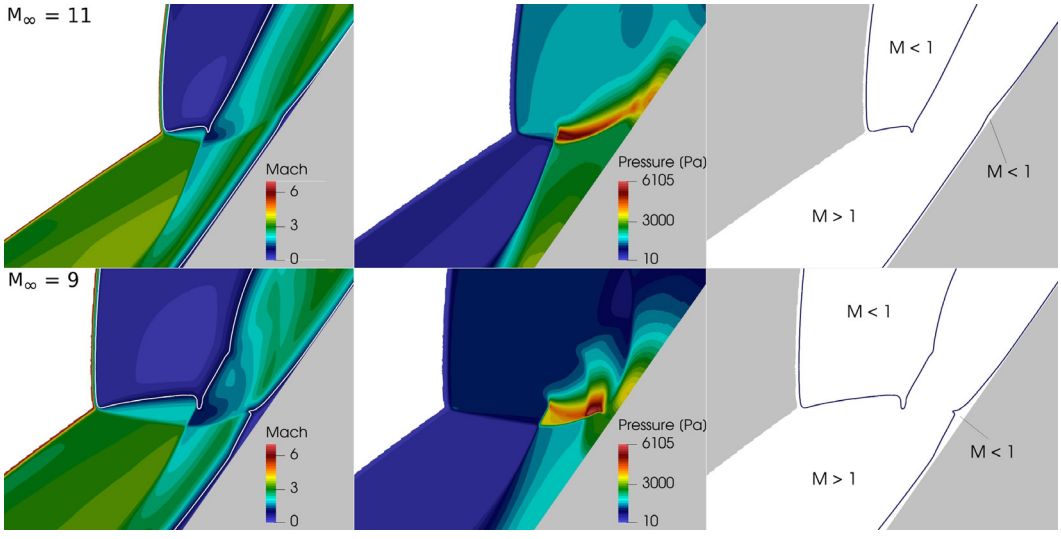

FIG. 24. Close-up in the region of main interaction: $M_\infty = 11$ (top) and $M_\infty = 9$ (bottom) for a CO_2-N_2 flow over the 15°–55° double-wedge. Reproduced with permission from Garbacz *et al.*, AIAA Paper No. 2022-3277 (2022). Copyright 2022 by the American Institute of Aeronautics and Astronautics.[18]

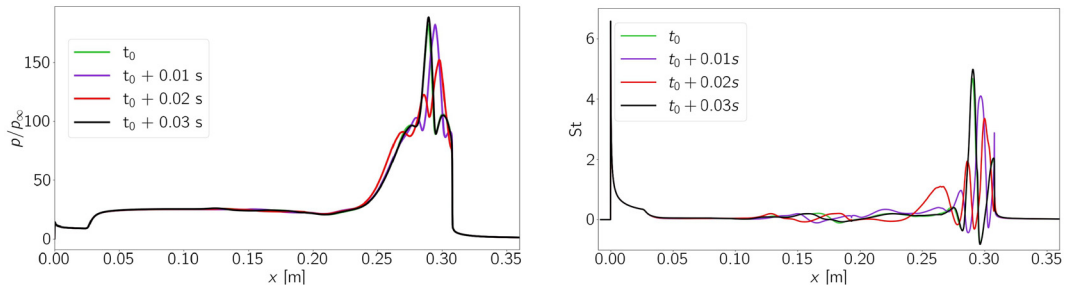

FIG. 25. Instantaneous surface quantities distribution for the $M_\infty = 7$ flow over the 15°–55° geometry: Normalized pressure (left) and Stanton number (right). Reproduced with permission from Garbacz *et al.*, AIAA Paper No. 2022-3277 (2022). Copyright 2022 by the American Institute of Aeronautics and Astronautics.[18]

pressure increase in the region 0.235–0.270 m). The Stanton number distribution is slightly more difficult to analyze in the main region of interaction due to the numerous local minima and maxima associated with reattachment and separation regions. However, the fluctuations in the vicinity of the compression corner are a strong indicator of the unsteady vortex dynamics inside the recirculation bubble.

A comparison of surface properties for all 15°–55° Cases, Mach 11, 9, and 7 is shown in Fig. 26. For the unsteady case, a time average is plotted. The differences in the pattern of interaction between $M_\infty = 11$ and $M_\infty = 9$ are reflected on the distribution of surface quantities. Up until the compression corner at $x = 0.193$ m, the plots are qualitatively identical. For $M_\infty = 11$, downstream of the corner, the normalized surface pressure exhibits two peaks, associated with boundary layer reattachment and shock impingement. The Stanton number distribution follows the same behavior, with a significant decay between the two peaks, corresponding to boundary layer reattachment in the compression corner and shock induced boundary layer separation, respectively. The surface pressure of the $M_\infty = 9$ cases continuously increases from the first separation point at $x = 0.085$ m, as a result of the successive shocks: compression corner separation and detachment shocks, as well as separation and detachment shocks due to impingement. The Stanton number distribution for the case $M_\infty = 9$, at the bottom of Fig. 26, is also indicative of these four shocks: (1) flow separation due to the compression corner shown by the small peak and followed by decreasing Stanton number at $x = 0.088$ m, (2) subsequent reattachment peak at $x = 0.233$ m, (3) flow separation due to shock impingement indicated by the very narrow peak and subsequent decrease at $x = 0.238$ m, and (4) reattachment downstream of the region of shock impingement at $x = 0.243$ m.

Similarly to the previous geometries, decreasing freestream Mach number leads to overall lower distributions of surface normalized pressure and Stanton number. Even though the red line corresponds to a time-averaged solution, by looking at Fig. 25, we conclude that this is also the case for the instantaneous distributions. The maximum instantaneous normalized pressure is approximately 188 for $t_0 + 0.03$ s, which is 1.9 and 2.2 smaller than the largest peaks obtained for, respectively, $M_\infty = 9$ and $M_\infty = 11$. For the Stanton number, the maximum instantaneous value is 5 for $t_0 + 0.03$ s, which is 1.1 and 2 larger than maximum Stanton number values obtained, respectively, for $M_\infty = 9$ and $M_\infty = 11$.

In Fig. 26, it is also interesting to notice that the location of shock impingement travels upstream from $M_\infty = 11$ to $M_\infty = 9$, and downstream from $M_\infty = 9$ to $M_\infty = 7$. This is because between Mach 11 and 9 the size of the recirculation bubble and shock interaction pattern is quite similar, expect for the larger separation region in the location of impingement for $M_\infty = 9$, that pushes the triple-point and the region of main interaction upstream. From $M_\infty = 9$ to $M_\infty = 7$ the size of the recirculation bubble becomes much larger and the main region of the interaction, including shock impingement, occurs closer to the expansion corner. Particularly in the case of the Stanton number distributions, vortex dynamics in the recirculation bubble is indicated by the fluctuations of surface heating from approximately $x = 0.088$ to $x = 0.219$ m.

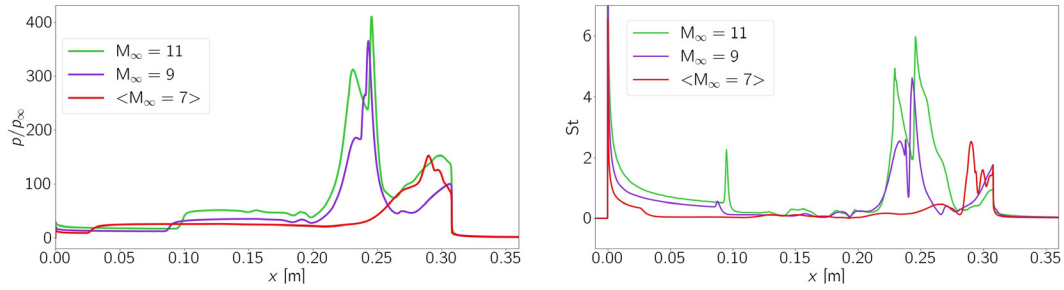

FIG. 26. Comparison of surface quantities distribution for different freestream Mach numbers for the 15°–55° geometry. For $M_\infty = 7$, the time average is plotted. Normalized pressure (left), Stanton number (right). Reproduced with permission from Garbacz *et al.*, AIAA Paper No. 2022-3277 (2022). Copyright 2022 by the American Institute of Aeronautics and Astronautics.[18]

VI. ROLE OF NONEQUILIBRIUM PROCESSES ON THE INTERACTION MECHANISMS

In this section, the role of nonequilibrium processes in defining the type of interaction is detailed in relation to the case of 15°–40° and 15°–45° wedges. The nonequilibrium effects in the case of the 15°–50° and 15°–55° Cases are conceptually equivalent to those of the 15°–45° geometry. For all cases, a measure of thermal nonequilibrium is given by the contours of $T - T_v$, with white regions indicating thermal equilibrium where $T - T_v \approx 0$ (Figs. 10, 15, 18, and 21).

As aforementioned, from the general theory of inviscid gas dynamics, higher Mach numbers tend to reduce the oblique shock angle and the bow shock standoff distance. When real effects play a significant role, this tendency is further emphasized: higher freestream Mach numbers lead to increasing nonequilibrium effects behind the shock, i.e., a larger amount of internal energy is transferred to the vibrational modes and dissociation reactions are more likely to occur, which overall contributes to increasing post-shock density and decreasing shock angles as well as the bow shock standoff distance.[8]

The flow revealed to be chemically frozen for all the three different Mach numbers since temperatures are not high enough to trigger dissociation. However, as seen at the bottom row of Fig. 10, the flowfield is in thermal nonequilibrium. The largest difference between translational and vibrational temperatures is obtained for $M_\infty = 11$, in the flow region just behind the bow shock. It is also for the case of higher Mach number that the difference between temperatures is the lowest further downstream as we approach the wall (dark blue contours for $M_\infty = 11$ vs cyan/blue contours for $M_\infty = 7$). This is due to the higher post-shock pressures resulting from higher freestream Mach number, that contribute to accelerating the process of internal energy transfer between translational and vibrational modes further downstream of the bow shock, as a result of a larger number of molecular collisions. Just downstream of the detachment shock there is another region of strong thermal nonequilibrium—stronger for higher freestream Mach—which, following the same reasoning, is due to larger post-shock translational temperatures resulting from the higher freestream Mach number. In the compression corner, contrary to what is observed downstream of the bow shock, the flow gets closer to a state of thermal equilibrium with decreasing freestream Mach number. Results show that thermal equilibrium tends to be reached in regions of separated flow, where viscous effects are dominant as well as the influence from the isothermal thermal equilibrium wall. The flow times scales associated with low subsonic velocities become much larger than the times associated with vibrational relaxation. As the separated flow region enlarges with decreasing freestream Mach number, there is more thermal equilibrium in the compression corner for lower freestream Mach.

For the 15°–45° case, most part of the flowfield is in thermal nonequilibrium, as seen at the bottom row of Fig. 15. Contrary to the 15°–40° double-wedge, regardless the value of Mach number, the flow displays some regions where thermal equilibrium is reached (white regions). Thermal equilibrium is seen for $M_\infty = 9$ and $M_\infty = 7$ in separated flow regions. It is also seen that larger portions of the domain are in thermal equilibrium near the compression corner. Toward the expansion corner, the opposite trend is observed: as Mach number increases, which results in higher post-shock pressures, the process of internal energy transfer between translational and vibrational modes accelerates, leading to larger regions of thermal equilibrium downstream of the bow shock.

When it comes to the 15°–50° and 15°–55° geometries, no major differences are seen in the parametric study regarding the behavior of thermal nonequilibrium effects, relative to the trends seen for the 15°–40° and 15°–45° geometries. The behavior of nonequilibrium effects in the context of viscous shock interaction patterns over double-wedges can be summarized as follows. There are mainly two effects playing a role in how thermal equilibrium is reached: low velocities causing flow times scale to become significantly larger than vibrational relaxation time scales; high pressures leading to more molecular collisions and therefore accelerating the process of energy exchange between vibrational and translational modes. Results have shown that

- just behind a shock, higher freestream Mach number leads to higher post-shock translational temperature, and therefore a larger difference between translational and vibrational temperature, which means stronger thermal nonequilibrium;
- as the energy exchange process gradually occurs downstream of a shock toward the wall/expansion corner, the effect of higher pressure obtained for higher Mach number seems to prevail, and the difference between temperatures (degree of thermal nonequilibrium) is smaller for higher freestream Mach number;
- in regions of separated flow, where viscous effects are dominant, as well as the influence from the isothermal thermal equilibrium wall, the effect of flow times scales becoming significantly larger than vibrational relaxation time scales due to subsonic velocity prevails. Because the separated flow region is larger for lower freestream Mach number, it is concluded that, in the compression corner, larger regions of thermal equilibrium are obtained for lower freestream Mach number.

VII. FINAL REMARKS

The theory of inviscid compressible fluid mechanics states that for a flow over a single wedge, increasing the freestream Mach number causes the oblique attached shock wave, or the detached bow shock, to move closer to the body. When real gas or high-temperature effects become relevant, this tendency is further emphasized: higher freestream Mach numbers lead to increased nonequilibrium conditions behind the shock, i.e., a larger amount of internal energy is transferred to the vibrational modes and dissociation reactions are more likely to occur, which overall contributes to increasing post-shock density and smaller shock angles and bow shock standoff distance. In the case of the flow over a double-wedge, which presents two compression corners, different shock waves interact with each other and complex non-linear changes in the flow are expected to take place when freestream conditions vary.

In this work, the effect of the changes in the freestream Mach number on the shock interaction patterns over four double-wedge geometries is investigated for carbon-dioxide flows. The parametric study revealed that, as the Mach number decreases, the size of flow separation regions increases. This resulted in additional detachment and reattachment shocks that change the types of flow pattern, as a consequence of the changes in the size of the bubble. It is concluded that decreasing the freestream Mach number has an effect on the pattern of interaction similar to the one of increasing the angle of the second wedge,[8] and contrary to the one of increasing the freestream temperature:[16] the recirculation bubble becomes larger leading to more complex and stronger mechanisms of interaction, characterized by larger shock angles and bow shock standoff distance. For larger aft

TABLE VI. Patterns of interaction—summary.

Geometry	$M_\infty = 11$	$M_\infty = 9$	$M_\infty = 7$
15°–40°	Type VI	Type VI	Type VI
15°–45°	Type VI	Type VI + type VI	Type VI + type VI
15°–50°	Type VI + type VI–type V transition with RR reflection	Type VI + type VI–type transition with RR reflection	Type VI + type V with RR reflection + shock impingement pattern
15°–55°	Type VI + type V with RR reflection	Type VI + type V with RR reflection + shock impingement pattern	Type VI + Unsteady oscillating type V between MR reflection and RR reflection + shock impingement pattern

angles, there seems to be a threshold of the Mach number below which the flow becomes unsteady. Table VI summarizes the shock interaction patterns obtained in the parametric study.

Changes in the aerothermal loads acting on the surface of the wedge reflect the changes in the interaction mechanism. The trends resulting from decreasing freestream Mach number seem to oppose to the ones resulting from increasing the aft wedge angle and the freestream temperature. Decreasing the Mach number leads to overall lower surface heating and pressure, as well as smaller regions of thermal equilibrium downstream of the bow shock toward the wall and the expansion corner. It is concluded that this is due to the higher post-shock pressures obtained for the higher Mach number, which accelerate the process of internal energy relaxation. To complete the parametric study with respect to all the relevant parameters that are expected to greatly impact shock interaction patterns, future work will look into exploring the effects of turbulence by changing the freestream Reynolds number.

ACKNOWLEDGMENTS

We wish to acknowledge the SU2-NEMO working group: Kyle Hanquist, Ozgur Tumuklu, Walter Maier, Michele Capriati, Thierry Magin and Jacob Needles for relevant comments and discussions.

AUTHOR DECLARATIONS

Conflict of Interest

The authors have no conflicts to disclose.

Author Contributions

Catarina Garbacz: Conceptualization (equal); Data curation (lead); Formal analysis (lead); Investigation (lead); Methodology (equal); Validation (equal); Visualization (lead); Writing – original draft (equal); Writing – review & editing (equal). **Fábio Morgado:** Methodology (equal). **Marco Fossati:** Conceptualization (equal); Formal analysis (supporting); Funding acquisition (lead); Investigation (supporting); Project administration (lead); Resources (lead); Supervision (lead); Writing – review & editing (supporting).

DATA AVAILABILITY

The data that support the findings of this study are available from the corresponding author upon request.

REFERENCES

[1]G. Tchuen, M. Fogue, Y. Burtschell, D. Zeitoun, and G. Ben-Dor, "Shock-on-shock interactions over double-wedges: Comparison between inviscid, viscous and nonequilibrium hypersonic flow," in *Shock Waves*, edited by K. Hannemann and F. Seiler (Springer, Berlin, Heidelberg, 2009), pp. 1497–1502.
[2]G. Tchuen, Y. Burtschell, and D. E. Zeitoun, "Numerical study of the interaction of type IVr around a double-wedge in hypersonic flow," Comput. Fluids **50**, 147–154 (2011).
[3]J. Li, Y. Zhu, and X. Luo, "Thermochemical non-equilibrium effects on type VI-V transition in hypersonic double-wedge flow," in *29th International Symposium on Shock Waves 1*, edited by R. Bonazza and D. Ranjan (Springer International Publishing, Cham, 2015), pp. 167–172.
[4]J. Olejniczak, M. Wright, and G. Candler, "Numerical study of inviscid shock interactions on double-wedge geometries," J. Fluid Mech. **352**, 1–25 (1997).
[5]A. S. Durna, M. El Hajj Ali Barada, and B. Celik, "Shock interaction mechanisms on a double wedge at Mach 7," Phys. Fluids **28**, 096101 (2016).
[6]P. Thirunavukkarasu and S. Ghosh, "Numerical simulation of high temperature effects on high enthalpy flow over double wedge geometry," AIAA Paper No. 2019-1904, 2019.
[7]D. Vatansever and B. Celik, "Unsteady shock interaction mechanisms of high enthalpy reacting flows over double wedges at Mach 7," Phys. Fluids **33**, 056110 (2021).
[8]C. Garbacz, F. Morgado, and M. Fossati, "Effect of thermal nonequilibrium on the shock interaction mechanism for carbon dioxide mixtures on double-wedge geometries," Phys. Fluids **34**, 026108 (2022).
[9]O. Tumuklu, D. A. Levin, and J. M. Austin, "Shock-shock interactions for a double wedge configuration in different gases," AIAA Paper No. 2015-1520, 2015.
[10]O. Tumuklu, D. A. Levin, S. F. Gimelshein, and J. M. Austin, "Factors influencing flow steadiness in laminar boundary layer shock interactions," AIP Conf. Proc. **1786**, 050005 (2016).
[11]C. Garbacz, W. Maier, J. Scoggins, T. Economon, T. Magin, J. Alonso, and M. Fossati, "Shock interactions in inviscid air and CO_2-N_2 flows in thermochemical non-equilibrium," Shock Waves **31**, 239–253 (2021).
[12]G. Pezzella, D. de Rosa, and R. Donelli, "Computational analysis of shock wave boundary layer interactions in non-equilibrium hypersonic flow," AIAA Paper No. 2015-3578, 2015.
[13]B. Edney, "Anomalous heat transfer and pressure distributions on blunt bodies at hypersonic speeds in the presence of an impinging shock," Report No. FFA-115 (The Aeronautical Research Institute of Sweden, Stockholm, 1968).
[14]A. Durna and B. Celik, "Time-periodic shock interaction mechanisms over double wedges at Mach 7," Shock Waves **29**, 381 (2019).
[15]A. S. Durna and B. Celik, "Effects of double-wedge aft angle on hypersonic laminar flows," AIAA J. **58**, 1689–1703 (2020).
[16]C. Garbacz, M. Fossati, W. Maier, J. J. Alonso, J. Scoggins, T. Magin, and T. D. Economon, "Numerical study of shock interference patterns for gas flows with thermal nonequilibrium and finite-rate chemistry," AIAA Paper No. 2020-1805, 2020.
[17]C. Park, "Review of chemical-kinetic problems of future NASA missions—I: Earth entries," J. Thermophys. Heat Transfer **7**, 385–398 (1993).
[18]C. Garbacz, F. Morgado, and M. Fossati, "Response of shock interaction patterns to different freestream conditions in carbon-dioxide flows over double-wedges," AIAA Paper No. 2022-3277, 2022.

[19]W. Xiong, J. Li, Y. Zhu, and X. Luo, "RR–MR transition of a Type V shock interaction in inviscid double-wedge flow with high-temperature gas effects," Shock Waves **28**, 751–763 (2018).
[20]C. L. Running, T. J. Juliano, J. S. Jewell, M. P. Borg, and R. L. Kimmel, "Hypersonic shock-wave/boundary-layer interactions on a cone/flare," Exp. Therm. Fluid Sci. **109**, 109911 (2019).
[21]P. Gnoffo, R. Gupta, and J. Shinn, "Conservation equations and physical models for hypersonic air flows in thermal and chemical nonequilibrium," NASA Technical Paper No. 2867 (1989), p.158.
[22]C. Park, J. T. Howe, R. L. Jaffe, and G. V. Candler, "Review of chemical-kinetic problems of future NASA missions—II: Mars entries," J. Thermophys. Heat Transfer **8**, 9–23 (1994).
[23]D. Liao, S. Liu, J. Huang, H. Jian, A. Xie, and Z. Wang, "Measurement and numerical simulation of shock standoff distances over hypersonic spheres in CO_2 in a ballistic range," Shock Waves **30**, 131–138 (2020).
[24]I. Armenise, P. Reynier, and E. Kustova, "Advanced models for vibrational and chemical kinetics applied to Mars entry aerothermodynamics," J. Thermophys. Heat Transfer **30**, 705–720 (2016).
[25]M. Camac, "CO_2 relaxation processes in shock waves," in *Fundamental Phenomena in Hypersonic Flow* (Cornell U.P., Ithaca, NY, 1966), pp. 195–215.
[26]J. B. Scoggins, V. Leroy, G. Bellas-Chatzigeorgis, B. Dias, and T. E. Magin, "Mutation++: MULticomponent Thermodynamic and Transport properties for IONized gases in C++," SoftwareX **12**, 100575 (2020).
[27]L. Landau and E. Teller, Physik Z. Sowjetunion **10**, 34 (1936).
[28]R. C. Millikan and D. R. White, "Systematics of vibrational relaxation," J. Chem. Phys. **39**, 3209–3213 (1963).
[29]C. Park, "Assessment of two-temperature kinetic model for ionizing air," J. Thermophys. Heat Transfer **3**, 233–244 (1989).
[30]J. B. Scoggins, "Development of numerical methods and study of coupled flow, radiation, and ablation phenomena for atmospheric entry," Ph.D. thesis (Von Karman Institute for Fluid Dynamics, 2017).
[31]J. D. Anderson, *Hypersonic and High-Temperature Gas Dynamics*, 3rd ed. (AIAA, 2019).
[32]C. R. Wilke, "A viscosity equation for gas mixtures," J. Chem. Phys. **18**, 517–519 (1950).
[33]A. Eucken, "Über das wärmeleitvermögen, die spezifische wärme und die innere reibung der gase," Phys. Z. **14**, 324–332 (1913).
[34]See https://github.com/su2code/SU2 for source code.
[35]T. D. Economon, F. Palacios, S. R. Copeland, T. W. Lukaczyk, and J. J. Alonso, "SU2: An open-source suite for multiphysics simulation and design," AIAA J. **54**, 828–846 (2016).
[36]See https://github.com/mutationpp/Mutationpp for source code.
[37]M.-S. Liou and C. J. Steffen, "A new flux splitting scheme," J. Comput. Phys. **107**, 23–39 (1993).
[38]A. G. Sebastian Willems and P. Seltner, "Shock-shock interaction test case," in ESA ATD3 Workshop (2018).
[39]F. Morgado, C. Garbacz, and M. Fossati, "Impact of anisotropic mesh adaptation on the aerothermodynamics of atmospheric reentry," AIAA J. **60**, 3973–3989 (2022).
[40]H. G. Hornung and G. H. Smith, "The influence of relaxation on shock detachment," J. Fluid Mech. **93**, 225–239 (1979).
[41]G. Candler, "Computation of thermo-chemical nonequilibrium Martian atmospheric entry flows," in 5th Joint Thermophysics and Heat Transfer Conference (1990).
[42]A. M. Knisely, "Experimental investigation of nonequilibrium and separation scaling in double-wedge and double-cone geometries," Ph.D. thesis (The University of Illinois at Urbana-Champaign, 2016).
[43]M. J. Wright, G. V. Candler, and D. Bose, "Data-parallel line relaxation method for the Navier-Stokes equations," AIAA J. **36**, 1603–1609 (1998).
[44]J. Li, Y. Zhu, and X. Luo, "On type VI-V transition in hypersonic double-wedge flows with thermo-chemical non-equilibrium effects," Phys. Fluids **26**, 086104 (2014).
[45]G. Kumar and A. De, "Role of corner flow separation in unsteady dynamics of hypersonic flow over a double wedge geometry," Phys. Fluids **33**, 036109 (2021).